This is a non-peer reviewed preprint submitted to EarthArXiv April 10th, 2021. The manuscript is currently being prepared for submission to Nature Geoscience. Subsequent versions of this manuscript may have different content. Please contact the corresponding author with any feedback.

Quantification of the hydrological control on speleothem oxygen isotopic variability

Pauline C. Treble[1,2*], Andy Baker[2,1], John C. Hellstrom[3], Nerilie J. Abram[4,5], Jagoda Crawford[1], Michael K. Gagan[6,7], Andrea Borsato[8], Alan Griffiths[1], Petra Bajo[9,3], Monika Markowska[10,1], Stacey Priestley[11,1], Stuart Hankin[1], David Paterson[12]

[1]ANSTO, Lucas Heights, 2234, Australia

[2]School of Biological, Earth and Environmental Sciences, UNSW Sydney, Kensington, 2052, Australia

[3]School of Earth Sciences, University of Melbourne, Parkville, 3010, Australia

[4]Research School of Earth Sciences, Australian National University, Canberra, 2601, Australia

[5]ARC Centre of Excellence for Climate Extremes, Australian National University, Canberra, 2601, Australia

[6]School of Earth, Atmospheric and Life Sciences, University of Wollongong, 2522, Australia

[7]School of Earth and Environmental Sciences, The University of Queensland, Brisbane, QLD, 4072

[8]School of Environmental and Life Sciences, University of Newcastle, Callaghan, 2308, Australia

[9]Croatian Geological Survey, Zagreb, Croatia

[10]Max Planck Institute for Chemistry, Mainz, 55128, Germany

[11]School of Physical Sciences, University of Adelaide, 5005, Australia

[12]Australian Synchrotron ANSTO, Clayton, 3168, Australia

*Corresponding author: pauline.treble@ansto.gov.au

Speleothems have long been regarded as state-of-the-art materials for terrestrial paleoclimate reconstruction owing to their potential for precisely dated chronologies and preservation of detailed oxygen isotopic ($\delta^{18}O$) records that are routinely interpreted as a proxy for hydroclimate. Yet replicated speleothem $\delta^{18}O$ records from the same cave do not always agree, posing a conundrum: if these records are reliable they should exhibit a common isotopic response to hydroclimate forcing. Using a meta-analysis of a global database of speleothem $\delta^{18}O$ records, as well as published dripwater data, we show that disagreement between replicated records is common and is consistent with in-cave variability in drip $\delta^{18}O$ that is unrelated to climate, cave depth or lithology. We present a case study of new coeval stalagmite $\delta^{18}O$ records from Golgotha Cave in southwest Australia, where the isotopic differences between four stalagmites that grew during the last eight centuries are informed by long-term monitoring of the cave. It is demonstrated that karst hydrology is a major driver of within cave speleothem and drip $\delta^{18}O$ variability, primarily due to the influence of fractures on flowpath variability. Applying this understanding assists in moving towards quantitative reconstruction of past climate variability from speleothem $\delta^{18}O$ records globally.

Oxygen isotopes are a well-studied tracer of water and thus the hydrological cycle[1-3]. Preservation of O isotopes within paleoenvironmental archives provides an opportunity to study past hydroclimatic variability[4] as well as climate dynamics with external forcing different to the present[5,6]. Speleothems are excellent paleoclimate archives owing to their potential for continuous, high resolution $\delta^{18}O$ data with well-constrained chronologies occurring over most climatic zones where limestone karst exists (e.g., refs[7,8]). These properties have motivated the collation of speleothem $\delta^{18}O$ records into global databases[9-11] that facilitate regional synthesis of these data to identify past climate patterns[12]; and promote data-model comparisons to evaluate the performance of climate models across different past climate states[13].

Measurement of speleothem $\delta^{18}O$ is routine, and these values reflect the isotopic composition of source water (meteoric precipitation) and cave temperature[14]. However, speleothem $\delta^{18}O$ may not always be an ideal proxy for hydroclimate owing to variable karst flowpaths between water falling as meteoric precipitation and emerging as dripwater within a cave[15]. Additional processes can also influence the fractionation of $^{18}O/^{16}O$ between dripwater and calcite[14]. In the quest to reach quantitative reconstruction of climate variability from speleothem $\delta^{18}O$, increasing attention has been focused on constraining the latter[16-18] while the impact of flowpaths is less widely acknowledged. Some studies have utilised karst hydrology models to simulate the potential for karst store volume, infiltration thresholds and flow type to impact dripwater $\delta^{18}O$ (refs. [19,20]); but validation of the impact of these processes on the speleothem record is limited by a lack of studies where speleothem $\delta^{18}O$ has been constrained by cave monitoring, with exceptions (refs.[21-26]).

The recognised complexities of speleothem $\delta^{18}O$ means that replication of speleothem records from the same cave or karst region is considered the 'gold standard' in assessing their robustness as paleo-environmental archives[12,27]. Yet it is evident that coeval time series frequently do not replicate in detail – often displaying differences in mean, variability and trends (e.g., refs. [28,29]). Studies using coeval records commonly create 'master' or 'composite' records by splicing techniques that scale records according to mean values[30,31] or apply a filter through merged datasets[32,33]. The application of largely arbitrary data corrections may result in loss of information, including the statistical mean $\delta^{18}O$ value that is a critical target for model performance (e.g. ref. [34]), as well as the loss of opportunity for further quantification of hydroclimatic information if a more mechanistic understanding of flowpaths was applied[35].

Here, we quantify the within-cave range of mean $\delta^{18}O$ values using global datasets of dripwater[36] and speleothems[11]. For speleothems, we utilised the SISAL V2 database[11] to identify caves with multiple speleothem $\delta^{18}O$ time series containing overlapping chronologies. We then improve our understanding of the processes giving rise to different mean values for dripwater $\delta^{18}O$ between flowpaths through a case study of coeval speleothem records from Golgotha Cave (southwest Australia; Fig. 1). Uniquely, within the Golgotha Cave system dripwater hydrochemistry is well-constrained by long-term monitoring[37,38] and flowpaths have been characterised by a spatially dense network of automated drip loggers and lidar mapping[39-41]. This setting allows us to, for the first-time, robustly assess the role that karst hydrology plays in determining the $\delta^{18}O$ variability between coeval speleothem paleoclimate records.

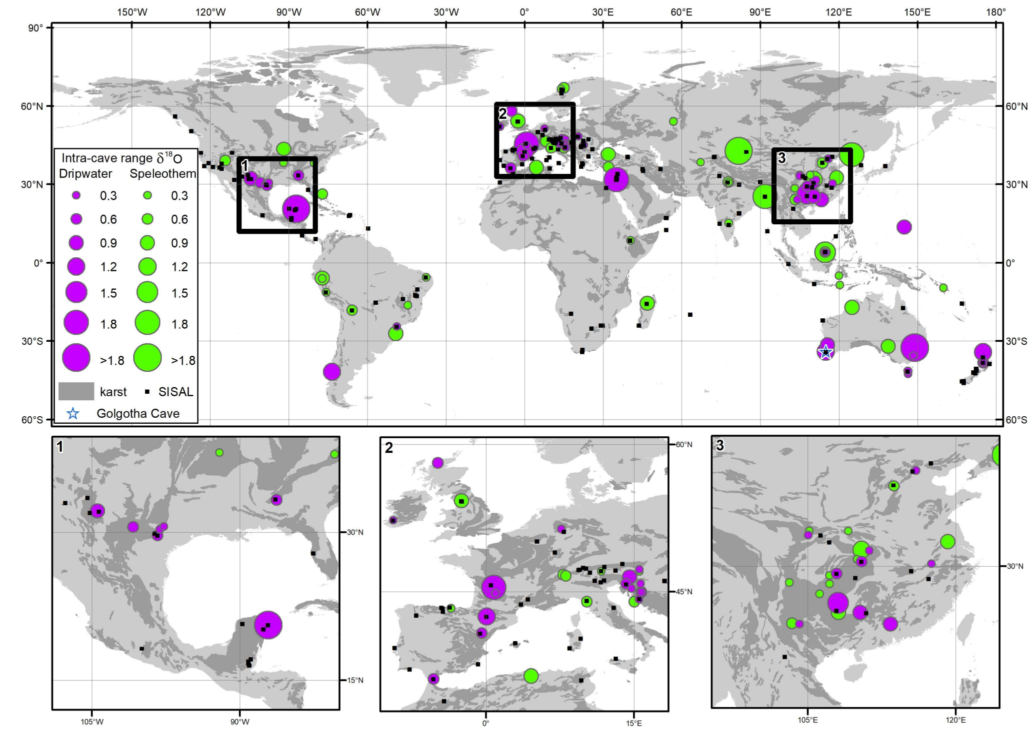

Fig. 1. Locations of caves used in global meta-analysis of dripwater and speleothem datasets with the range of mean $\delta^{18}O$ values indicated by symbol size for coeval dripwater and/or coeval speleothems from these caves. Location of Golgotha Cave and other sites from the SISAL V2 database are also shown. Darker grey shading indicates karst regions[42].

Global speleothem and drip $\delta^{18}O$ assessment. The within cave range of mean $\delta^{18}O$ values were assessed globally for 50 caves with 229 drip monitoring sites, and 64 caves with 192 paired coeval speleothem time-series (Fig. 1; Supplementary Tables 1-2; Methods). We find that the range of mean $\delta^{18}O$ values is greater than analytical uncertainty for 52% of caves that have coeval dripwater monitoring and 39% of caves that have coeval speleothem records (Fig. 2). Analytical uncertainty is set at 0.3 ‰ based on inter-laboratory comparisons[43,44]. As each coeval dataset will likely come from an individual laboratory where routine reproducibility can be several times better (e.g. typically 0.06 ‰ – see Methods), our analysis is conservative. Thus our findings imply that within cave variability in mean $\delta^{18}O$ values is common worldwide and is similar in magnitude whether assessed via dripwater or speleothem data; the difference between the means for the within cave range for dripwater versus speleothems was insignificant (0.5 $‰_{VSMOW}$ versus 0.4 $‰_{VPDB}$; p-value=0.35). This suggests that the majority of within cave variability between speleothem $\delta^{18}O$ records may be attributed to differences in flowpaths within the karst above the cave. We further demonstrate that this occurs on a global scale, independent of hydroclimate or other potential factors such as host rock geology or cave depth (see Supplementary Figs. 1 and 2). Additionally, no relationship was found between the range of mean speleothem $\delta^{18}O$ values and the distance from the cave entrance (Supplementary Fig. 1) further supporting that the difference in speleothem mean $\delta^{18}O$ may be inherited from the dripwater rather than the potential influence of cave microclimate instability on the isotopic fractionation between dripwater and speleothem.

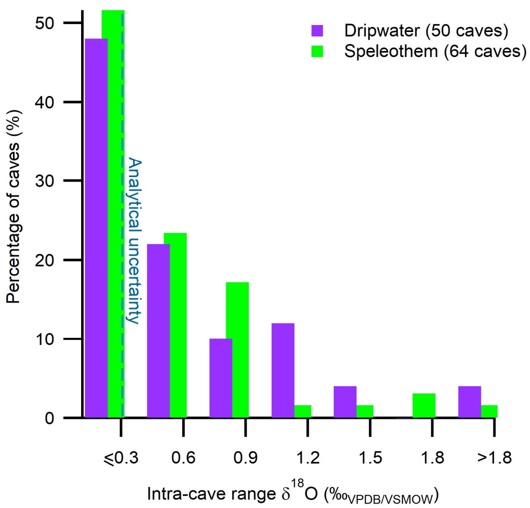

Fig. 2. Histogram of the range of mean $\delta^{18}O$ values for each cave determined from the global meta-analysis of dripwater and speleothem datasets.

A global mean of 0.4 ‰$_{VPDB}$ for the within cave range of mean speleothem $\delta^{18}O$ is large and thus there is a need to further explore the underlying mechanism. The lack of caves with both coeval drip monitoring and coeval speleothem data precludes using existing data to directly assess the role of within cave dripwater $\delta^{18}O$ variability in explaining mean speleothem $\delta^{18}O$ variability. Just four caves in this global meta-analysis have both datasets[28,45-50] and only one exceeds our analytical threshold[46,47]. This highlights the need for more coeval speleothem datasets from monitored caves in order to objectively quantify the hydrological control on speleothem $\delta^{18}O$ variability.

Golgotha Cave case study. To assess the importance of karst hydrological flowpaths driving variability in mean $\delta^{18}O$ between coeval speleothems we use a case study of four stalagmite records that grew during the last eight centuries from Golgotha Cave, SW Australia (Fig. 3a). Dripwater monitoring commenced after each stalagmite was removed and varies in length from 5 to 14 years duration. This represents a unique dataset to interrogate the influence of intra-cave differences in karst flow on individual speleothem $\delta^{18}O$ records over a period when cave temperature can expect to have remained relatively constant.

Annual dripwater $\delta^{18}O$ mean values differ by up to 1 ‰$_{VSMOW}$ between monitoring sites within Golgotha Cave[36]. Conversion of drip $\delta^{18}O$ to calcite equivalent values, using calcites farmed during our monitoring study (Supplementary Text and Supplementary Table 3), demonstrates that drip $\delta^{18}O$ gives a viable extension of the individual speleothem records associated with each drip (Fig. 3b) and that the offset between speleothem $\delta^{18}O$ is primarily driven by differences in drip $\delta^{18}O$ values. The isotopic differences between the four speleothems persist throughout the 800 years of coeval data (Fig. 3a), but with differences in temporal evolutions that in the absence of consideration of karst processes could otherwise be misinterpreted to represent very different hydroclimate histories.

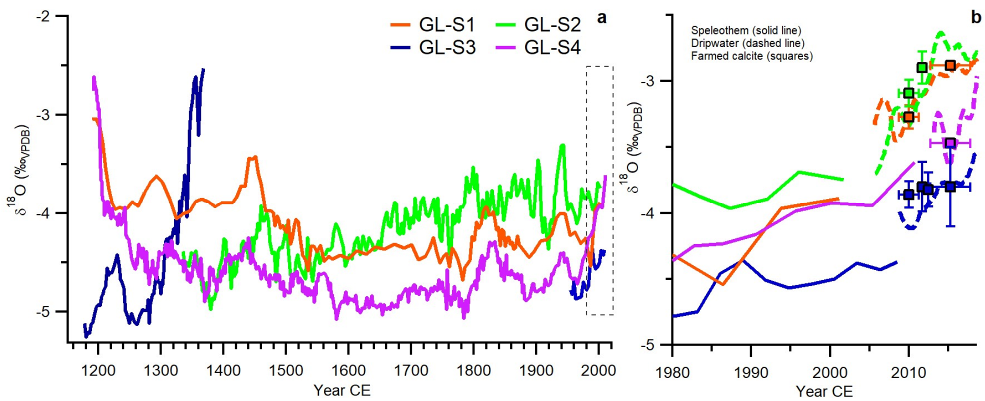

Fig. 3a,b. Golgotha Cave speleothem records (a), comparison between speleothem, dripwater and farmed calcite for recent decades (b). Dashed box indicates region re-plotted in (b). Dripwaters were converted to calcite equivalent values using an empirical bulk fractionation factor derived from calcites farmed at the drip sites (Supplementary Text and Supplementary Table 3). Dripwater (calcite equivalent $\delta^{18}O$ values) are used to extend the speleothem time series. The agreement (allowing for the rising trend) also supports the empirical fractionation factor calculated from Golgotha farmed calcites and dripwaters.

Variability in mean drip $\delta^{18}O$ associated with recharge thresholds and karst store behaviour can account for the differences observed in the $\delta^{18}O$ values of coeval speleothems within Golgotha Cave. Lidar mapping of the karst system at Golgotha Cave, coupled with a network of 34 automated high frequency drip loggers[40], has provided a detailed understanding of water storage and flowpaths that enables interpretation of the varying ways that hydroclimate signals emerge in the cave system through dripwater $\delta^{18}O$. The majority of water movement to the ceiling of Golgotha Cave is via flow through the matrix of the host-rock[41] and is characterised by low drip rates with low $\delta^{18}O$ variability[37,40]. But some flowpaths exhibit a different behaviour, displaying a threshold rise in drip rate in response to activation of flow along a fracture[40], while a third flow type termed 'combination' has flow through an interconnected network of fractures and fissures/conduits[41]. Drips feeding the stalagmites in this study represent this range of flow types: predominately matrix (GL-S1, GL-S2), matrix plus fracture (GL-S4) and combination (GL-S3) (Fig. 4a-c). Field campaigns conducted to determine the $\delta^{18}O$ value of drips across the automated drip loggers[40] demonstrate a significant isotopic distinction between matrix flow (-4.0±0.1 ‰, 1σ; n=58) versus fracture flow (-4.7±0.1 ‰, n=22) classified drips (Fig. 4c).

A fracture activation episode is evident in the monitoring time series for stalagmite GL-S4 as an abrupt 115% increase in drip rate during November 2013 (Fig. 4a,b). This occurred in response to a wet season with rainfall above the 90th percentile, and is consistent with rapid, deep delivery of infiltrating rainwater along a fracture[40,51]. The increase in flow was accompanied by a 0.5 ‰$_{VSMOW}$ decrease in $\delta^{18}O$ values of the drip for GL-S4 over the subsequent year (Fig. 4c). These dripwater values are isotopically consistent with larger rainfall events, which have relatively lower $\delta^{18}O$ values owing to the 'amount effect' in this region[52]. The drip monitoring suggests that the relative volume of water contributed by large rainfall events to karst reservoirs is amplified by fractures and is related to the size and/or number of contributing fractures. The drip rate response for the 'combination' flowpath (GL-S3) similarly rises in 2013, only here the larger network of permeable features[40] smooths the response to infiltration. Dripwater $\delta^{18}O$ values for this site are the lowest of the four monitored sites, and 1 ‰$_{VSMOW}$ lower than precipitation-weighted rainfall $\delta^{18}O$ (Fig. 4c), consistent with the karst store for GL-S3 being sustained largely by infiltration via fractures.

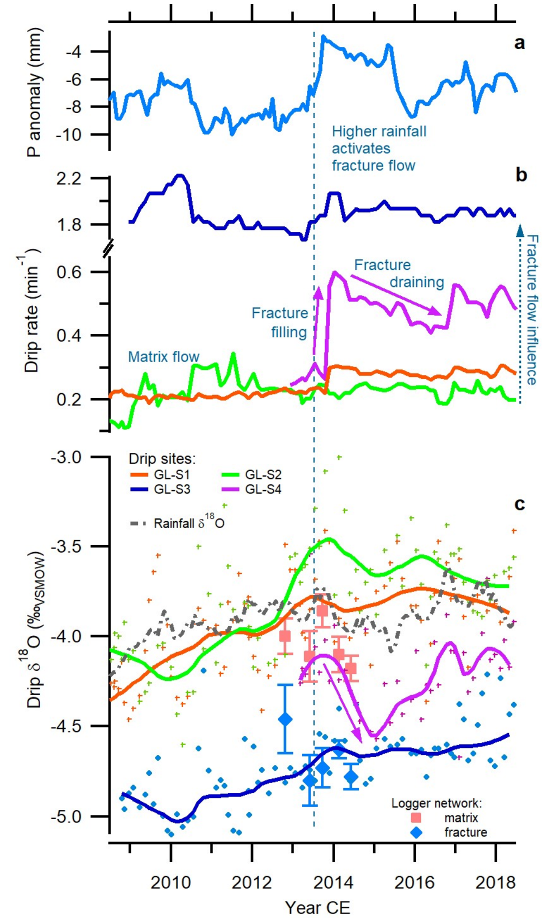

Fig. 4a-c. Golgotha Cave monitoring data. Smoothed monthly precipitation (P) anomalies (a), monitored drip rate (b) precipitation–weighted monthly rainfall δ^{18}O and smoothed dripwater δ^{18}O (c) for drip sites where speleothems were collected. Shown also on panel (c) are the mean δ^{18}O values of matrix and fracture flow sites from drips in the automated logger network obtained during five separate sampling campaigns each conducted over 2-5 day durations between 2012 and 2014. Monthly precipitation anomalies were calculated using the monthly climatological means from 1950 to 2020. An exponentially-weighted moving average (EWMA) was applied to monthly P anomalies with a half-life parameter of 36.6 months; similarly an EWMA was applied to monthly rainfall δ^{18}O using a 25 month half-life, as well as a lag of 19 months supported by our field studies in ref.[40,53]. Dripwater δ^{18}O were smoothed with a loess 2^{nd} order filter (span 0.3). Drip rates exhibit a threshold response to higher infiltration indicating the fracture component of each flowpath[40]. For example, the drip for GL-S4 rapidly increases in response to higher precipitation anomalies during 2013 compared to the much smaller rise in the drip rate for GL-S1, indicating that a larger fracture component is feeding GL-S4. Over the same period, mean drip rate of the logger network increased from 0.16±0.02 to 0.20±0.40 for matrix flow sites and from 2.21±0.40 to 8.32±3.43 for fracture flow sites. The relative contribution of fracture flow to each drip site is inversely related to drip δ^{18}O values with activation of fractures occurring during periods of higher infiltration associated with lower rainfall δ^{18}O values.

The extensive monitoring and characterisation of the Golgotha Cave system (see also Supplementary Text) allows us to interpret the differences between the mean values of Golgotha Cave δ^{18}O speleothem records as well as the drivers of the variability through time. Records GL-S1 and GL-S4 have similar isotopic trends on multi-decadal to multi-centennial scales throughout the last eight centuries; however, GL-S4 is isotopically offset by approximately -0.5 ‰$_{VPDB}$ (Fig. 3a). This is consistent with our identification of GL-S4 receiving a larger component of fracture flow whilst GL-S1 as supplied predominately by matrix flow. Oxygen isotopic values for stalagmite GL-S1 do not fall below -4.5 ‰$_{VPDB}$, whereas they are typically below this value for GL-S4 (Fig. 3b). This indicates that selective recharge due to fracture activation during periods of higher rainfall was a persistent process impacting the flow pathway, hence the $\delta^{18}O$ record, of GL-S4. Further support for this process-based understanding is the typical widening of the isotopic offset between the two records that is observed during periods of relatively lower $\delta^{18}O$ values (Fig. 3a), indicative of enhanced fracture activation feeding GL-S4 in response to more intense rainfall. Additionally, from 1990 CE onwards, all records and their extended dripwater time series display rising $\delta^{18}O$ trends. This implies a reduction in fracture flow, i.e., conditions were insufficient to overcome recharge threshold(s) for regular fracture activation[51] and is consistent with the sustained rainfall decrease in this region that began around 1970 CE[54].

Stalagmite GL-S2 $\delta^{18}O$ values are initially similar to GL-S4 from 1330 to 1440 CE, intermittent between GL-S1 and GL-S4 until 1560 CE, then at or above GL-S1 for the remainder of the speleothem and dripwater record (Fig. 3a,b). Temporal flow-switching was documented previously for GL-S2's drip site[57] and is consistent with its location in the cave characterised as having high-spatial heterogeneity in flow regime[40]. In contrast, stalagmites GL-S1 and GL-S4 come from a section of the cave with low spatial variability in flow-paths attributed to their connectedness to the common hydrological domain of the matrix[39,40].

Speleothems from drips that are dominated by 'combination' or complex fracture flowpaths show greater isotopic variability and less reliable growth consistent with their drip supplied by flow along fractures rather than the matrix. Speleothem GL-S3 experienced discontinuous growth over the last 800 years (Fig. 3a), with rejuvenation of growth commencing with low $\delta^{18}O$ values (e.g. 1200-1300 and 1950s CE; Fig. 3a). This is consistent with flow to this speleothem dominated by fracture flowpaths[40] that require relatively high infiltration from larger rainfall events to activate[51]. A relatively wet interval during the 13th century is supported by falling d18O values supplied by the matrix to GL-S1 plus fracture activation initiating growth to stalagmites GL-S2 and GL-S4. An enhanced non-linear response to recharge is also evident in GL-S3: $\delta^{18}O$ values are up to 1 ‰$_{VPDB}$ lower than the other records at 1200-1300 CE but display a rising trend that is initially similar in value to GL-S4 until approximately 1300 CE when GL-S3 $\delta^{18}O$ values steeply rise a further 1.5 ‰$_{VPDB}$ in less than three decades, exceeding the matrix-flow record (GL-S1; Fig. 3a). The continuity of all the other records at the time when GL-S3 ceases growing (approx. 1360 CE) indicates that infiltration to the cave system is still occurring, although not to the karst store(s) supplying GL-S3. The isotopic maximum prior to termination of this growth phase: -2.5 ‰$_{VPDB}$ ($\delta^{18}O$; Fig. 3a) is similar to observed dripwater maxima (Fig. 3b), thus could be inherited from the dripwater, or additional processes may be dominating speleothem $\delta^{18}O$ as the store volume in this 'stranded' reservoir depletes, including enhanced isotopic disequilibrium effects as the drip interval lengthens[55,56].

Implications for quantified hydroclimate reconstructions. The Golgotha Cave case study demonstrates that the differences between coeval speleothem $\delta^{18}O$ records from the same cave can be controlled by flowpaths. The global meta-analysis reveals that such within cave variability is common worldwide. The global mean of $\delta^{18}O$ offsets between drip sites in caves (0.6 ‰) is similar in magnitude to that observed in Golgotha Cave. The global mean of within cave isotopic range for coeval speleothems is 0.4 ‰. While we have not considered isotopic fractionation that can further impact speleothem $\delta^{18}O$ values during calcite precipitation in the SISAL data, the evidence presented here suggests that the karst hydrological control is an important factor in explaining within-cave speleothem $\delta^{18}O$ differences.

A previous global meta-analysis on monitored cave datasets[36] showed that dripwater $\delta^{18}O$ values are close to that of rainfall at cooler locations, while reflecting recharge rather than rainfall $\delta^{18}O$ at warmer locations. Building on this, our expanded global meta-analysis, demonstrates that the additional impacts of karst hydrological heterogeneity is important over all climate types and karst characteristics. Golgotha Cave hydrology experiences matrix flow through the highly porous

Pleistocene aeolinite host rock[37]. Globally, most karst is older and retains little or no primary porosity, hence water movement is likely to be more impacted by heterogeneities in flowpaths through fractures. In mature limestones, a high density of fissures, sediment-filled structures and paleokarst could similarly act as porous media; and drips with matrix flow properties have been identified in many monitored caves from mature limestones (e.g. refs.[26,58,59])

Speleothems associated with complex fractures are likely to show highly non-linear responses to hydroclimate forcing and more caution should be taken with interpreting paleoclimate information from them whereas speleothems dominated by matrix flowpaths and simple fracture structures are likely to be more suitable. Where coeval records exist, the difference in mean $\delta^{18}O$ value could be viewed from a process-based understanding that may enable quantitative hydroclimate reconstructions. For example, temporal changes in this mean value records such as GL-S1 and GL-S4, could be exploited to identify past changes in rainfall characteristics, with larger offsets representing periods of enhanced recharge from larger rainfall events. Furthermore, interpretation alongside a karst model that is able to reconcile the $\delta^{18}O$ offset between coeval speleothems arising from recharge thresholds and differences in flowpaths would allow for the possibility of reconstructing mean precipitation $\delta^{18}O$, which is directly comparable to output from general circulation models.

Methods

Global meta-analysis. The dripwater dataset of ref.[36] was extended to include studies with: 1. at least quarterly sampling over 12 months; and 2. sites that had not previously meet the criteria of having nearby rainfall $\delta^{18}O$ data. Mean $\delta^{18}O$ for each drip site over a 12 month period was calculated and the range of these mean values for each cave was determined (Supplementary Table 1). We utilised the SISAL V2 database[11] to identify caves with speleothem $\delta^{18}O$ records satisfying the following criteria: 'mineralogy' = calcite AND coeval interval exceeds 10% of the minimum age of overlap AND overlap interval exceeds 2x'lin_interp_age_uncert_pos' of the maximum age AND 2x'lin_interp_age_uncert_neg' of the minimum age AND each section contain >10 $\delta^{18}O$ measurements (Supplementary Table 2). Hiatuses were accounted for and if present, the record split into growth intervals and each growth interval treated as a potential record. The mean $\delta^{18}O$ value for each speleothem pair was calculated for the period of overlap (Supplementary Table 2) and the within cave range calculated. A conservative threshold value of 0.3‰ was chosen for analytical uncertainty based on inter-laboratory studies[43] and consistent with the value previously adopted[36].

Golgotha Cave dripwater data. Drip data presented here are an extension of published data[37] and new dripwater data collected at the speleothem GL-S4 (2012-19). Methods for dripwater data appear in ref.[37] with the exception of $\delta^{18}O$ measurements being made using Picarro L2120-I Water Analyser at ANSTO (see ref.[60] for method) from 2012 onwards. Supplementary Table 4 contains identification codes for dripwater and speleothem pairing and summarises site data.

Carbonate stable isotopes. Each speleothem was milled along the growth axis using a Taig micromill to produce homogenised powders representing increments of 0.1 to 0.2 mm, depending on the speleothem growth rate. Powders were weighed to 180–220 µg and analysed for $\delta^{18}O$ and $\delta^{13}C$ using a Finnigan MAT-251 isotope ratio mass spectrometer coupled to a Kiel I carbonate device, or a Thermo MAT-253 isotope ratio mass spectrometer coupled to a Kiel IV carbonate device (using 110–130 µg samples), at the Research School of Earth Sciences, ANU. Analyses were calibrated using NBS-19 standard ($\delta^{18}O_{V\text{-}PDB}$ = −2.20 ‰ and $\delta^{13}C_{V\text{-}PDB}$ = 1.95 ‰). A further linear correction for $\delta^{18}O$ measurements was carried out using the NBS-18 standard ($\delta^{18}O_{V\text{-}PDB}$ = −23.0 ‰). The original delta values for NBS-19 and NBS-18 are used to maintain consistency of results through time in the RSES Stable Isotope Facility. Long-term precision of both the MAT-251 and MAT-253 instruments is ±0.06 ‰ for $\delta^{18}O$ and ±0.04 ‰ for $\delta^{13}C$ (±1σ standard deviation).

Speleothem chronologies. Speleothem chronologies were determined using U-series disequilibrium dating at the University of Melbourne, and are supported by 'bomb pulse' radiocarbon dating previously published in ref.[61] and/or laminae counting of annual Sr concentrations mapped by X-ray fluorescence microscopy (XFM) at the XFM beamline at the Australian Synchrotron. Full details of chronologies and U-series disequilibrium data are given in the Supplementary Information.

Online supporting material

Supporting figures, tables, text and associated references, are contained in the Supplementary Information.

Data availability

Acknowledgements

This research is supported by funding from the Australian Research Council (DP140102059 to PCT and NJA) and a Land & Water Australia grant (ANU52). The micro-XRF analysis research was undertaken on the X-ray fluorescence microscopy (XFM) beamline at the Australian Synchrotron, part of ANSTO under proposals PA13457 and PA14312. We used the SISAL database, made possible through the Speleothem Isotope Synthesis and Analysis (SISAL) working group of the Past Global Changes (PAGES) project, supported by the Swiss Academy of Sciences and the Chinese Academy of Sciences. We gratefully acknowledge the assistance from the staff at Calgardup Caves (Department of Biodiversity, Conservations and Attractions) to conduct the cave monitoring, as well as Fabio Oriani for assistance with image processing of synchrotron maps and technical support from Barbora Gallagher, Jennifer van Holst, Joe Cali, Joan Cowley, Heather Scott-Gagan, Jennifer Wurtzel and Lewis Adler.

Author contributing statement

This manuscript was devised and written by PCT and ABaker. All co-authors contributed to the writing of the paper. Golgotha Cave speleothem and monitoring data were created by PCT with input from JCH, PB, NJA, ABorsato, MM, DJP, MKG and ABaker. JC, ABaker, PCT, SP and SH conducted the analysis for Figure 1.

References

1 Dansgaard, W. Stable isotopes in precipitation. *Tellus* **4**, 436-468 (1964).

2 Gat, J. R. Atmospheric water balance—the isotopic perspective. *Hydrological Processes* **14**, 1357-1369, doi:10.1002/1099-1085(20000615)14:8<1357::AID-HYP986>3.0.CO;2-7 (2000).

3 Brady, E. *et al.* The Connected Isotopic Water Cycle in the Community Earth System Model Version 1. *Journal of Advances in Modeling Earth Systems* **11**, 2547-2566, doi:10.1029/2019MS001663 (2019).

4 Petit, J. R. *et al.* Climate and atmospheric history of the past 420,000 years from the Vostok ice core, Antarctica. *Nature* **399**, 429-436, doi:10.1038/20859 (1999).

5 Liu, Z. *et al.* Evolution and forcing mechanisms of El Niño over the past 21,000 years. *Nature* **515**, 550-553, doi:10.1038/nature13963 (2014).

6 Clark, P. U. *et al.* Oceanic forcing of penultimate deglacial and last interglacial sea-level rise. *Nature* **577**, 660-664, doi:10.1038/s41586-020-1931-7 (2020).

7 Cheng, H. *et al.* The Asian monsoon over the past 640,000 years and ice age terminations. *Nature* **534**, 640-646, doi:10.1038/nature18591 (2016).

8 Partin, J. W., Cobb, K. M., Adkins, J. F., Clark, B. & Fernandez, D. P. Millennial-scale trends in west Pacific warm pool hydrology since the Last Glacial Maximum. *Nature* **449**, 452-456, doi:10.1038/nature06164 (2007).

9 Bolliet, T. *et al.* Water and carbon stable isotope records from natural archives: a new database and interactive online platform for data browsing, visualizing and downloading. *Clim. Past* **12**, 1693-1719, doi:10.5194/cp-12-1693-2016 (2016).

10 Atsawawaranunt, K. *et al.* The SISAL database: a global resource to document oxygen and carbon isotope records from speleothems. *Earth Syst. Sci. Data* **10**, 1687-1713, doi:10.5194/essd-10-1687-2018 (2018).

11 Comas-Bru, L. *et al.* SISALv2: A comprehensive speleothem isotope database with multiple age-depth models. *Earth Syst. Sci. Data* **12**, 2579-2606, doi:10.5194/essd-12-2579-2020 (2020).

12 Comas-Bru, L. & Harrison, S. Bringing Added Value to Speleothem Research. *Quaternary* **2**, 7 (2019).

13 Comas-Bru, L. *et al.* Evaluating model outputs using integrated global speleothem records of climate change since the last glacial. *Clim. Past* **15**, 1557-1579, doi:10.5194/cp-15-1557-2019 (2019).

14 Hendy, C. The isotope geochemistry of speleothems-I. The calculation of the effects of different modes of formation on the isotopic composition of speleothems and their applicability as palaeoclimatic indicators. *Geochimica et Cosmochimica Acta* **35**, 802-824 (1971).

15 Bradley, C., Baker, A., Jex, C. N. & Leng, M. J. Hydrological uncertainties in the modelling of cave drip-water d18O and the implications for stalagmite palaeoclimate recontructions. *Quaternary Science Reviews* **29**, 2201-2214, doi:doi:10.1016/j.quascirev.2010.05.017 (2010).

16 Mickler, P. J., Stern, L. A. & Banner, J. L. Large kinetic isotope effects in modern speleothems. *Geological Society Of America Bulletin* **118**, 65-81 (2006).

17 Hansen, M., Scholz, D., Schöne, B. R. & Spötl, C. Simulating speleothem growth in the laboratory: Determination of the stable isotope fractionation (δ13C and δ18O) between H2O, DIC and CaCO3. *Chem Geol* **509**, 20-44, doi:https://doi.org/10.1016/j.chemgeo.2018.12.012 (2019).

18 Guo, W. & Zhou, C. Patterns and controls of disequilibrium isotope effects in speleothems: Insights from an isotope-enabled diffusion-reaction model and implications for

quantitative thermometry. *Geochim Cosmochim Ac* **267**, 196-226, doi:https://doi.org/10.1016/j.gca.2019.07.028 (2019).

19 Baker, A. & Bradley, C. Modern stalagmite delta (super 18) O; instrumental calibration and forward modelling. *Global and Planetary Change* **71**, 201-206.

20 Jex, C. N., Phipps, S. J., Baker, A. & Bradley, C. Reducing uncertainty in the climatic interpretations of speleothem δ18O. *Geophysical Research Letters* **40**, 2259-2264, doi:10.1002/grl.50467 (2013).

21 Bar-Matthews, M., Ayalon, A., Kaufman, A. & Wasserburg, G. J. The Eastern Mediterranean paleoclimate as a reflection of regional events: Soreq cave, Israel. *Earth and Planetary Science Letters* **166**, 85-95 (1999).

22 Spotl, C., Fairchild, I. J. & Tooth, A. F. Cave air control on dripwater geochemistry, Obir Caves (Austria): Implications for speleothem deposition in dynamically ventilated caves. *Geochimica Et Cosmochimica Acta* **69**, 2451-2468 (2005).

23 Mattey, D. P. *et al.* in *Tufas and Speleothems: unravelling the microbial and physical controls* Vol. 336 (eds H M Pedley & M Rogerson) 323-344 (The Geological Society of London, London, 2010).

24 Tremaine, D. M., Froelich, P. N. & Wang, Y. Speleothem calcite farmed in situ: Modern calibration of delta O-18 and delta C-13 paleoclimate proxies in a continuously-monitored natural cave system. *Geochimica et Cosmochimica Acta* **75**, 4929-4950, doi:Doi 10.1016/J.Gca.2011.06.005 (2011).

25 Riechelmann, D. F. C. *et al.* Monitoring Bunker Cave (NW Germany): A prerequisite to interpret geochemical proxy data of speleothems from this site. *Journal of Hydrology* **409**, 682-695, doi:Doi 10.1016/J.Jhydrol.2011.08.068 (2011).

26 Pape, J. R., Banner, J. L., Mack, L. E., Musgrove, M. & Guilfoyle, A. Controls on oxygen isotope variability in precipitation and cave drip waters, central Texas, USA. *Journal of Hydrology* **385**, 203-215 (2010).

27 Dorale, J. A. & Liu, Z. H. Limitations of Hendy Test Criteria in Judging the Paleoclimatic Suitability of Speleothems and the Need for Replication. *Journal of Cave and Karst Studies* **71**, 73-80 (2009).

28 Fohlmeister, J. *et al.* Bunker Cave stalagmites: an archive for central European Holocene climate variability. *Climate of the Past* **8**, 1751-1764 (2012).

29 Cai, Y. *et al.* Variability of stalagmite-inferred Indian monsoon precipitation over the past 252,000 y. *Proceedings of the National Academy of Sciences* **112**, 2954, doi:10.1073/pnas.1424035112 (2015).

30 Lachniet, M. S. Climatic and environmental controls on speleothem oxygen isotope values. *Quaternary Science Reviews* **28**, 412-432, doi:10.1016/j.quascirev.2008.10.021 (2009).

31 Carolin, S. A. *et al.* Varied Response of Western Pacific Hydrology to Climate Forcings over the Last Glacial Period. *Science* **340**, 1564-1566 (2013).

32 Williams, P. W., King, D. N. T., Zhao, J. X. & Collerson, K. D. Speleothem master chronologies: combined Holocene O-18 and C-13 records from the North Island of New Zealand and their palaeoenvironmental interpretation. *Holocene* **14**, 194-208 (2004).

33 Ayliffe, L. K. *et al.* Rapid interhemispheric climate links via the Australasian monsoon during the last deglaciation. *Nature Communications* **4**, 2908, doi:10.1038/ncomms3908 (2013).

34 Caley, T., Roche, D. M., Waelbroeck, C. & Michel, E. Oxygen stable isotopes during the Last Glacial Maximum climate: perspectives from data–model (<i>i</i>LOVECLIM) comparison. *Clim. Past* **10**, 1939-1955, doi:10.5194/cp-10-1939-2014 (2014).

35 Hartmann, A. & Baker, A. Modelling karst vadose zone hydrology and its relevance for paleoclimate reconstruction. *Earth-Science Reviews* **172**, 178-192, doi:https://doi.org/10.1016/j.earscirev.2017.08.001 (2017).

36 Baker, A. *et al.* Global analysis reveals climatic controls on the oxygen isotope composition of cave drip water. *Nat Commun* **10**, 2984, doi:10.1038/s41467-019-11027-w (2019).
37 Treble, P. C. *et al.* An isotopic and modelling study of flow paths and storage in Quaternary calcarenite, SW Australia; implications for speleothem paleoclimate records. *Quaternary Science Reviews* **64**, 90-103 (2013).
38 Treble, P. C. *et al.* Impacts of cave air ventilation and in-cave prior calcite precipitation on Golgotha Cave dripwater chemistry, southwest Australia. *Quaternary Sci Rev* **127**, 61-72, doi:Doi:10.1016/j.quascirev.2015.06.001 (2015).
39 Mahmud, K., Mariethoz, G., Baker, A. & Treble, P. C. Hydrological characterization of cave drip waters in a porous limestone: Golgotha Cave, Western Australia. *Hydrological and Earth System Sciences* **22**, 977-988, doi:https://doi.org/10.5194/hess-22-977-2018 (2018).
40 Mahmud, K. *et al.* Estimation of deep infiltration in unsaturated limestone environments using cave LiDAR and drip count data. *Hydrological and Earth System Sciences* **20**, 359-373, doi:doi:10.5194/hess-20-359-2016 (2016).
41 Mahmud, K., Mariethoz, G., Treble, P. C. & Baker, A. Terrestrial LiDAR survey and morphological analysis to identify infiltration properties in the Tamala Limestone, Western Australia. *IEEE Journal of Selected Topics in Applied Earth Observations and Remote Sensing* **8**, 4871-4881, doi:10.1109/JSTARS.2015.2451088 (2015).
42 BGR, IAH, KIT & UNESCO. World Karst Aquifer Map. (WHYMAP, BGR, Hanover, 2017).
43 Ostermann, D. R. & Curry, W. B. Calibration of stable isotopic data: An enriched d18O standard used for source gas mixing detection and correction. *Paleoceanography* **15**, 353-360 (2000).
44 Wassenaar, L. I. *et al.* Seeking excellence: An evaluation of 235 international laboratories conducting water isotope analyses by isotope-ratio and laser-absorption spectrometry. **32**, 393-406, doi:10.1002/rcm.8052 (2018).
45 Boch, R. *Stalagmites from Katerloch Cave, Austria: Growth dynamics and high-resolution records of climate change* PhD thesis, Leopold-Franzens-Universitat Innsbruck, (2008).
46 Baker, A. & Bradley, C. Modern stalagmite delta (super 18) O; instrumental calibration and forward modelling. *Global and Planetary Change* **71**, 201-206 (2011).
47 Fuller, L. *et al.* Isotope hydrology of dripwaters in a Scottish cave and implications for stalagmite palaeoclimate research. *Hydrol. Earth Syst. Sci.* **12**, 1065-1074 (2008).
48 Moreno, A. *et al.* New speleothem data from Molinos and Ejulve caves reveal Holocene hydrological variability in northeast Iberia. *Quaternary Research* **88**, 223-233, doi:10.1017/qua.2017.39 (2017).
49 Riechelmann, S. *et al.* Sensitivity of Bunker Cave to climatic forcings highlighted through multi-annual monitoring of rain-, soil-, and dripwaters. *Chem Geol* **449**, 194-205, doi:https://doi.org/10.1016/j.chemgeo.2016.12.015 (2017).
50 Moreno, A. *et al.* Climate controls on rainfall isotopes and their effects on cave drip water and speleothem growth: the case of Molinos cave (Teruel, NE Spain). *Climate Dynamics* **43**, 221-241, doi:10.1007/s00382-014-2140-6 (2014).
51 Ireson, A. M., Butler, A. B. & Wheater, H. S. Evidence for the onset and persistence with depth of preferential flow in unsaturated fractured porous media. *Hydrology Research* **43**, 707-719, doi:10.2166/nh.2012.030 (2012).
52 Fischer, M. J. & Treble, P. C. Calibrating climate-delta O-18 regression models for the interpretation of high-resolution speleothem delta O-18 time series. *Journal Of Geophysical Research-Atmospheres* **113**, D17103, doi:10.1029/2007JD009694 (2008).
53 Leopold, M., Gupanis-Broadway, C., Baker, A., Hankin, S. & Treble, P. Time lapse electric resistivity tomography to portray infiltration and hydrologic flow paths from surface to cave. *Journal of Hydrology* **593**, 125810, doi:https://doi.org/10.1016/j.jhydrol.2020.125810 (2021).

54 Hope, P., Timbal, B. & Fawcett, R. Associations between rainfall variability in the southwest and southeast of Australia and their evolution through time. *Int. J. Climatol.* **30**, 1360-1371 (2010).

55 Mühlinghaus, C., Scholz, D. & Mangini, A. Modelling fractionation of stable isotopes in stalagmites. *Geochim Cosmochim Ac* **73**, 7275-7289, doi:https://doi.org/10.1016/j.gca.2009.09.010 (2009).

56 Deininger, M. & Scholz, D. ISOLUTION 1.0: an ISOtope evoLUTION model describing the stable oxygen (δ18O) and carbon (δ13C) isotope values of speleothems. *Int J Speleol* **48**, 3, doi:https://doi.org/10.5038/1827-806X.48.1.2219 (2019).

57 Fitzsimmons, K. E. *et al.* Late Quaternary palaeoenvironmental change in the Australian drylands. *Quaternary Sci Rev* **74**, 78-96, doi:Doi 10.1016/J.Quascirev.2012.09.007 (2013).

58 Ayalon, A., Bar-Mathews, M. & Sass, E. Rainfall-recharge relationships within a karstic terrain within the Eastern Mediterranean semi-arid region, Israel: d18O and dD charateristics. *Journal of Hydrology* **207**, 18-30 (1998).

59 Nava-Fernandez, C. *et al.* Pacific climate reflected in Waipuna Cave drip water hydrochemistry. *Hydrol. Earth Syst. Sci.* **24**, 3361-3380, doi:10.5194/hess-24-3361-2020 (2020).

60 Crawford, J., Hollins, S. E., Meredith, K. T. & Hughes, C. E. Precipitation stable isotope variability and subcloud evaporation processes in a semi-arid region. *Hydrological Processes* **31**, 20-34, doi:10.1002/hyp.10885 (2017).

61 Markowska, M. *et al.* Modelling the 14C bomb-pulse in young speleothems using a soil carbon continuum model. *Geochim Cosmochim Ac* **261**, 342-367, doi:https://doi.org/10.1016/j.gca.2019.04.029 (2019).

Supplementary Information

Quantification of the hydrological control on speleothem oxygen isotopic variability

Treble P.C. et al.

The Supplementary Information comprises:

Supplementary Text

Supplementary Tables

Supplementary Figures

Supplementary references

Supplementary Text

Farmed calcites and conversion of dripwater $\delta^{18}O$ to calcite equivalent values.

Two substrate types were used to collect modern calcite ('farmed calcites') that formed contemporaneously with the dripwater monitoring. Prior to 2013 these were discs machined from Delrin® plastic rod with approximate dimensions of 25 mm diameter and 4 mm thickness and sand-blasted to increase surface roughness and promote calcite precipitation. Following the introduction of acoustic drip loggers into each funnel, the substrate was switched to inverted watch glasses with roughened convex surface that could be placed on top of the logger and still permit acoustic transmission. Approximately 25-50 µg of carbonate was scraped from the substrates directly into the reaction thimbles. This was repeated to reproduce duplicate or triplicate measurements where possible and an average calculated (Supplementary Table 4). Samples were measured on the MAT-253 isotope ratio mass spectrometer with Kiel carbonate device at the Mark Wainwright Analytical Centre at UNSW Sydney according to the method in ref[1]. Data are normalised to the Vienna Pee Dee Belemnite (VPDB) scale using NBS19 ($\delta^{18}O$=−2.20‰ and $\delta^{13}C$=+1.95‰) and NBS-18 ($\delta^{18}O$=−23.0‰ and $\delta^{13}C$=−5.0‰). An isotopic fractionation factor ($\alpha_{calcite\text{-}water}$) was calculated using the equation:

$$\alpha_{calcite-water} = \frac{1 + \frac{\delta_{calcite}}{1000}}{1 + \frac{\delta_{water}}{1000}}$$

where $\delta_{calcite}$ is the farmed calcite $\delta^{18}O$ and δ_{water} is the corresponding mean drip water $\delta^{18}O$ value over the corresponding period each substrate was in the cave. δ_{water} is converted to the equivalent value on the VPDB scale using the equation $\delta^{18}O_{VPDB}$ = 0.97001* $\delta^{18}O_{VSMOW}$ -29.99.

Dripwater $\delta^{18}O$ measurements were converted from the VSMOW scale to a calcite equivalent on the VPDB scale using the average calculated isotopic fractionation factor (1.0318 ± 0.0004) and mean monthly cave temperature measured at Golgotha Cave (14.6±0.1°C; May 2017-July 2020).

Assessment of evaporation on dripwater $\delta^{18}O$

The range of mean dripwater $\delta^{18}O$ values accounts for the range in mean speleothem $\delta^{18}O$ values indicating that the differences between Golgotha Cave speleothems is primarily driven by dripwater $\delta^{18}O$. Our long-term monitoring demonstrates that the isotopic differences between flowpaths is attributable to the balance between matrix and fracture flow for each flowpath. Treble et al. (2013) ruled out the impact of evaporation within the karst as a driver of dripwater $\delta^{18}O$ as the dripwater $\delta^{18}O$ values are the same or lower than incoming rainfall. Here, we further address the alternative hypothesis that evaporation of water on stalactites could account for higher dripwater $\delta^{18}O$ at our slower dripping sites by examining relative humidity and pan evaporation data from Golgotha Cave. Average monthly relative humidity values were calculated from data originally acquired at 15 min intervals using a Datataker DT80 logger between May 2017 and July 2020 using a Vaisala HMP155 with Humicap 180RC and sensor warming enabled to negate saturation of the sensor at high humidity (accuracy $\pm$1.8%). High relative humidity is maintained throughout the year with an average of 98.9% (range 95.7 to 100%). Evaporation pans consisting of 95 mm diameter petri dishes glasses in triplicate were placed near our dripwater monitoring site in chamber 1 over two years (May 2012 – March 2014). Pans were filled with 70 mls of tapwater using a measuring cylinder. The volume of water lost was measured every six weeks when the pans were emptied and refilled. The average evaporation rate was 0.009 mm day^{-1} (range 0.002 to 0.019 mm day^{-1}; n=13).

We modelled the isotopic impact of evaporation on a thin film assuming a worse-case scenario whereby water flows exclusively on the outer surface of a stalactite and an evaporation rate of 0.1 mm day^{-1}. Assuming a drip volume, $V_d = 0.2$ mL, the water flux is

$$Q = \frac{V_d}{\tau}$$

where τ is the interval between drips. The evaporation rate inside the cave, $E = 0.1\text{mm/day}$, so the evaporation flux from water film over the stalagmite is

$$Q_E = EA_f$$

where A_f is the surface area of the film. Assuming that $Q_E \ll Q$, so that $Q + Q_E \approx Q$, the fraction of water which remains in the liquid phase is

$$f_l = 1 - \frac{Q_E}{Q}.$$

Modelling the stalactite as a cylinder with length 6 cm and diameter 1 cm, based on measurements of stalactites at this site[2], and assuming $\tau = 300s$ we obtain

$$f_l = 99.67\%.$$

To calculate isotopic fractionation, we assume that kinetic fractionation can be neglected because of the high humidity of the cave. With this condition, the result from Rayleigh Fractionation applies[3] which, for this system where vapour is removed, is written

$$R = R_0 f_l^{1/\alpha - 1}$$

where α is the equilibrium fraction factor, $\alpha = 1.0101$ at 16°C[4], R is the ratio of heavy-to-light isotopes, and R_0 is the initial R of the infiltrating water. Setting R_0 to equal standard VSMOW, using $f_l = 99.67$ calculated above, and converting to δ notation,

$$\delta_l = 0.03‰.$$

Thus, assuming a worse-case scenario of evaporation that is 5x higher than our observed value results in an estimated increase in dripwater $\delta^{18}O$ of 0.03‰, that is too weak by a factor of >10 to explain drip $\delta^{18}O$ variability.

<u>Assessment of disequilibrium and/or kinetics on speleothem $\delta^{18}O$</u>

Speleothem fabrics determined from thin section analysis shows that all stalagmites are columnar and open-columnar fabrics (see for fabric descriptions ref[5]) with no fabrics associated with "disequilibrium deposition" such as dendritic, micrite, microsparitic fabrics, detected.

Disequilibrium and/or kinetic isotopic effects result in a $\alpha_{calcite\text{-}water}$ value that departs from a value determined under conditions of thermodynamic equilibrium. Supplementary Table 4 shows that the $\alpha_{calcite\text{-}water}$ values calculated from our farmed calcites are consistent across the monitored Golgotha Cave drip sites (1.0318±0.0004) and the range in measured $1000\ln\alpha_{calcite\text{-}water}$ values between sites is <0.2‰. This demonstrates that disequilibrium and/or kinetic isotopic effects are not responsible for the difference in farmed calcites values over the monitored interval and we infer not responsible for the differences in mean speleothem $\delta^{18}O$. Rather, the difference in mean speleothem $\delta^{18}O$ values for Golgotha Cave are dominated by the difference in dripwater $\delta^{18}O$ values and this is driven by the ratio of matrix to fracture flow along a flowpath. Possible exceptions to this, as raised in the main text, are the interval 1300-1360 CE in GL-S3. We investigate this further below by investigating the relationship between speleothem $\delta^{13}C$ versus $\delta^{18}O$ which has been used as a possible diagnostic of disequilibrium and/or kinetic isotopic effects[6].

Scatterplots for Golgotha speleothems are shown in Supplementary Figure 3. Speleothem growth with lowest slope values and least co-variation between $\delta^{13}C$ and $\delta^{18}O$ occurs when $\delta^{18}O$ values are lowest, i.e., during times of persistent fracture flow in these speleothem records (e.g., 1200-1300 CE for GL-S3 and 1580-1790 CE GL-S4; see main text). Highest slope and co-variation are observed for speleothem GL-S3 during 1300-1360 CE when GL-S3 $\delta^{18}O$ values rapidly rise and exceed neighbouring matrix flow speleothems by at least 1 ‰. As outlined in the main text, this isotopic maximum precedes a growth hiatus and is interpreted to represent processes that could occur once a karst store is disconnected from infiltration and subsequently drains. This could include enhanced disequilibrium and/or kinetic isotopic fractionation between speleothem calcite and its source water as the drip interval lengthens. From 1180 to 1260 CE, GL-S1 and GL-S4 have high, declining $\delta^{18}O$ values (Fig. 3a; main text) as well as high slope and r^2 values (Supplementary Figure 3). Prior to this, GL-S1 sustained mean $\delta^{18}O$ value of -2.6±0.3‰ for a multi-centennial period. Regardless of the driver of these GL-S1 $\delta^{18}O$ values during this period, the high value as well as lack of growth in the other three stalagmites supports an extended dry period. This indicates that the downward trending values for GL-S1 and GL-S4 prior to 1200 CE are likely associated with establishment of new or reliable water percolation along a flow path. Thus the high values prior to 1200 CE and the high slope and r^2 values could indicate enhanced disequilibrium and or kinetic isotope fractionation due to very low drip rates or the incorporation of older water with high $\delta^{18}O$ values as a result of having been disconnected from infiltration during a dry period. Speleothems that are dominated by matrix flow either because they lack a significant fracture flow path (GL-S1) or during periods when the ratio of fracture to matrix flow is reduced (e.g. 1260-1580 GL-S4) have intermediate slope and r^2 values (Supplementary Figure 3). Speleothems have different mean $\delta^{13}C$ values (Fig. 3a,c) supporting mean speleothem $\delta^{13}C$ is related to speleothems being fed by different flowpaths as outlied in the main text. Speleothem $\delta^{13}C$ is also smoothly varying through time (Fig. 3c) supporting an environmental not kinetic control. Combining observations that variability in speleothem $\delta^{18}O$ values are driven by fracture activation and that the strength of the relationship between speleothem $\delta^{18}O$ and $\delta^{13}C$ also varies according to flow type, raises the possibility that dripwater $\delta^{13}C$ may also be influenced by conditions within a flow path, except when dripwater becomes disconnected from infiltration.

<u>Golgotha Cave speleothem chronologies</u>

X-ray fluorescence microscopy (XFM) maps were acquired on the speleothem polished slabs at 2 µm resolution (pixel size) at the XFM beamline at the Australian Synchrotron[7,8] using a monochromatic incident energy of 18.5 keV focussed to spot size of 1.5 µm, and dwell per pixel from 1 to 4 ms. The XFM elemental maps were created and analysed using GeoPIXE software, quantified by using single element Mn, Fe and Pt foils (Micromatter, Canada) and corrected by using a Ca matrix factor. Laminae counting and error estimate was made by determining the position of the Sr peaks on two parallel areas of the Sr maps at three confidence levels (> 95%, 50-95% and <50% confidence) using ImageJ software package according to the method outlined in ref.[9].

U-Th age measurements followed the method of ref[10]. Briefly, calcite wafers weighing 100-200 mg were dissolved and equilibrated with a mixed ^{229}Th-^{233}U-^{236}U tracer before U and Th are extracted in a single solution using Eichrom TRU resin before measurement on a Nu Plasma multi-collector ICPMS where isotope ratios of both elements are measured simultaneously. A ratio of initial [$^{230}Th/^{232}Th$] = 0.33±0.25 was applied and is defined by modelling the ratio required to bring ages into age-depth order for each stalagmite. This ratio is further supported by comparing the U/Th ADM to the laminae chronology for stalagmite GL-S4.

Age depth models were constructed by combining information from the date of collection, bomb pulse chronology[11], laminae counting of Sr maps and U/Th ages. The specific approach for each stalagmite is summarised in Supplementary Table 7.

Supplementary Table 1: Global dripwater data and meta-data. Range of mean dripwater $\delta^{18}O$ and climate meta-data were published in ref.[12] and references therein, unless otherwise indicated. Geology codes: L=limestone, D=dolomite, M=marble, MX=mixed and U=unknown. AI is aridity index.

Cave	Latitude	Longitude	Elevation (m)	Geology	Mean depth (m)	MAT (C)	P (mm)	PET (mm)	AI	Range mean $\delta^{18}O$ (‰)
Xianren Cave	24° 07' N	104° 08' E	1443	MX	90	16.7	1143	1280	0.76	0.30
Baojinggong Cave	24° 07' N	113° 21' E	610	L	170	21.2	1836	1325	1.39	0.80
Liangfeng Cave	26° 16' N	108° 03' E	600	L	110	18.5	1212	1121	1.12	1.40
Furong Cave	29° 13' N	107° 54' E	480	D	400	17.4	1027	1122	1.07	0.40
Penglaixian Cave	30° 14' N	117° 32' E	170	L	30	16.1	1781	1082	1.36	0.30
Heshang Cave	30° 27' N	110° 25' E	294	D	300	16.5	1343	1115	1.04	0.50
Wanwiang Cave	33° 10' N	105° 00' E	1200	L	140	14.9	461	1068	0.57	0.00
Shihua Cave	39° 47' N	115° 56' E	251	MX	80	12.2	539	992	0.59	0.10
Yongxing Cave	31° 35’ N	111° 14’ E	800	L	50	15.2	930	1051	0.98	0.20
Maomaotuo Big Cave[13]	25° 18' N	110° 16' E	209	MX	150	19.5	1885	493	1.39	0.65
Uamh an Tartair	58° 8' N	4° 56' W	220	D	10	7.1	1955	493	2.39	0.41
Bunker Cave	51° 22‘ N	7° 40' E	184	L	23	9.8	973	708	1.21	0.11
Postojna Cave	45° 47' N	14° 12' E	535	U	40	8.7	1590	813	1.62	0.38
Nova Grgosova Cave	45° 49' N	15° 40' E	239	L	8	11.2	1116	887	1.2	0.10
Lokvarka Cave	45° 21' N	14° 45' E	780	L	85	8.3	2256	739	1.86	0.20
Lower Barać Cave	44° 59' N	15° 43' E	310	L	32	11.2	1319	895	1.31	0.10
Upper Barać Cave	44° 59' N	15° 43' E	332	L	12	11.2	1319	895	1.31	0.40
Modrič Cave	44° 15' N	15° 32' E	32	L	8	16.1	1207	1026	0.97	0.10
Obir Cave	46° 31' N	14° 33' E	1090	L	53	6.8	1350	723	1.69	1.13
Beke Cave[14]	48° 29' N	20° 31' E	338	U		8.3	665	845	0.72	0.30
Ascunsa Cave[15]	45° 10' N	22° 37' E	1080	MX	145	14.1	980	662	1.48	0.06
Katerloch Cave[16]	47° 15' N	15° 33' E	900	L		8	1008	732	1.35	0.26
Crag Cave	52° 15' N	9° 26' W	80	U	23	11.3	1449	624	2	0.30
Seso Cave	42° 27' N	0° 02' E	794	U		13.8	905	907	0.81	1.16
Molinos Cave	40° 47’ N	0° 27' W	1050	L	20	13.2	434	893	0.6	0.32
Proumeyssac	44° 53' N	0° 56' E	152	U		13.6	984	985	0.87	0.13
Grotte de Villars	45° 26' N	0° 47' E	175	L	27.6	12.4	1005	963	0.96	1.39
St Michaels Cave[17]	36° 09' N	5° 21' W		U		18.3	767	1068	0.7	0.74
Soreq Cave[18,19]	31° 45' N	35° 01' E	400	D	20	20	500	1436	0.32	0.66
Westcave	30° 20' N	98° 8' W	250	L	23	20	813	1484	0.55	0.02
Inner Space Cavern	30° 36' N	97° 41' W	182	MX	15	19.2	848	1453	0.58	0.00

Caverns of Sonora	30° 33' N	100° 49' W		MX	28	17.9	536	1574	0.34	0.46
Natural Bridge Cavern	29° 41' N	98° 20' W	315	MX	43	19.6	740	1478	0.55	0.39
DeSoto Caverns[20]	33° 18' N	86° 17' W		D	20	17.2	1417	1414	1.01	0.29
Indian Oven Cave[21]	41° 54' S	73° 30' W	300	MX	15	9	1145	999	1.13	1.00
Carlsbad Caverns[22]	32 11' N	104 27' 'W	1000	L	350	14	390	1427	0.23	0.80
Jinapsan Cave	13° 24' N	144° 30' E	30	U		26	2600	1261	1.86	0.40
Wind Cave	4° 02' N	114° 48' E		U		25	3842	1472	2.61	0.40
Santana Cave[23]	24° 31' S	48° 43' W	250	L	300	18.6	1631	1414	0.97	0.30
Rio Secreto Cave	20° 35' N	87° 08' W		MX	7	25.8	1463	1601	0.82	3.10
Cathedral Cave	32° 37'S	148° 56' E	325	L	325	18.2	629	1461	0.45	1.94
Golgotha Cave	36° 5'S	115° 3' E	72	O	36	14.75	1113	1046	1.06	0.95
Harrie Wood Cave	35° 43'S	148° 29' E	965	L	34	11.1	1177	1098	1.07	0.21
Little Trimmer Cave	41° 33'S	146° 15' E	460	L		9.5	1061	860	1.68	0.00
Frankcombe Cave	42° 32'S	146° 27' E	400	L		8.3	1230	874	1.43	0.12
Wombeyan Caves[24]	34° 19'S	149° 58' E	600	M	1	9.7	823	1212	0.65	0.91
South Glory Cave[25,26]	35° 43'S	148° 29'E	900	L	40	10	1172	1098	1.07	0.10
Yonderup Cave[27]	31° 33' S	115° 41' E	25	O	4	15.1	725	1345	0.54	0.96
Aranui Cave[28]	38° 19''S	175° 01' E	395	L	50	12.8	1618	939	2.47	0.28
Waipuna Cave[29]	38° 19' S	175° 01' E	395	L	25	12.8	1408	939	2.47	0.12

Supplementary Table 2: Meta-data and mean $\delta^{18}O$ values of paired coeval speleothem data from SISAL database V2[30]. 'Age min' and 'Age max' represent the minimum and maximum age of the interval of overlap of each coeval dataset. See Methods for criteria used to calculated coeval data. Range in mean $\delta^{18}O$ values for each cave is shown in Figures 1 and 2 (main text).

Name	Site ID	Entity ID 1	Entity name 1	Entity ID 2	Entity name 2	Age min (ka)	Age max (ka)	Mean $\delta^{18}O$ (ID 1)	Mean $\delta^{18}O$ (ID 2)	Difference in mean $\delta^{18}O$ (‰)
Bittoo cave	1	1	BT-1	2	BT-2.1	25.13	29.21	-5.10	-5.38	0.28
Bittoo cave	1	1	BT-1	3	BT-2.2	43.83	56.20	-6.49	-5.92	0.57
Kesang cave	2	11	KS06-A-H	16	KS08-2-H	8.60	9.84	-11.77	-10.81	0.95
Kesang cave	2	11	KS06-A-H	622	CNKS-7	3.61	9.84	-11.07	-10.49	0.58
Kesang cave	2	11	KS06-A-H	623	CNKS-9	3.61	7.11	-10.82	-10.37	0.46
Kesang cave	2	12	KS06-A	15	KS08-1	76.17	85.06	-10.16	-9.15	1.01
Kesang cave	2	12	KS06-A	15	KS08-1	93.20	108.75	-8.79	-10.66	1.87
Kesang cave	2	12	KS06-A	15	KS08-1	189.11	234.85	-8.72	-8.85	0.13
Kesang cave	2	12	KS06-A	17	KS08-2	70.92	83.87	-9.83	-9.69	0.14
Kesang cave	2	12	KS06-A	17	KS08-2	94.98	104.60	-9.79	-11.34	1.54
Kesang cave	2	12	KS06-A	17	KS08-2	189.03	230.06	-9.26	-9.47	0.21
Kesang cave	2	13	KS06-B	15	KS08-1	257.35	292.00	-8.00	-7.74	0.26
Kesang cave	2	14	KS08-1-H	19	KS08-6	0.86	1.30	-7.08	-8.71	1.63
Kesang cave	2	14	KS08-1-H	620	CNKS-2	0.13	1.19	-7.46	-8.54	1.07
Kesang cave	2	14	KS08-1-H	621	CNKS-3	0.13	1.17	-7.48	-8.69	1.22
Kesang cave	2	14	KS08-1-H	622	CNKS-7	1.55	3.50	-9.37	-8.10	1.27
Kesang cave	2	14	KS08-1-H	623	CNKS-9	0.04	3.50	-8.54	-8.65	0.11
Kesang cave	2	15	KS08-1	17	KS08-2	187.13	230.08	-9.47	-9.38	0.09
Kesang cave	2	16	KS08-2-H	622	CNKS-7	8.60	10.12	-10.75	-10.55	0.20
Kesang cave	2	19	KS08-6	620	CNKS-2	0.86	1.20	-8.51	-8.90	0.39
Kesang cave	2	19	KS08-6	621	CNKS-3	0.86	1.17	-8.32	-9.03	0.71
Kesang cave	2	19	KS08-6	623	CNKS-9	0.88	1.31	-8.73	-8.03	0.70
Kesang cave	2	620	CNKS-2	621	CNKS-3	0.11	1.17	-8.50	-8.66	0.16
Kesang cave	2	620	CNKS-2	623	CNKS-9	0.12	1.20	-8.54	-8.08	0.46
Kesang cave	2	621	CNKS-3	623	CNKS-9	0.12	1.17	-8.66	-8.12	0.54
Kesang cave	2	622	CNKS-7	623	CNKS-9	1.55	7.06	-9.83	-9.99	0.16
Villars cave	4	27	Vil-stm6	29	Vil-stm11	6.68	8.55	-4.91	-4.63	0.28
Villars cave	4	27	Vil-stm6	33	Vil-stm1	0.40	2.29	-4.81	-4.41	0.41
Villars cave	4	28	Vil-stm9	30	Vil-stm14	32.03	51.74	-3.64	-4.16	0.52
Villars cave	4	28	Vil-stm9	31	Vil-stm27	31.60	49.30	-3.59	-3.82	0.24
Villars cave	4	30	Vil-stm14	31	Vil-stm27	32.04	49.30	-4.19	-3.82	0.37

Yangkou cave	5	35	YK12	38	YK61	139.99	172.93	-8.57	-8.76	0.18
Hulu cave	6	40	MSD	41	MSL	36.11	52.81	-7.71	-7.89	0.17
Hulu cave	6	42	PD	43	YT	14.41	17.21	-5.25	-6.10	0.85
Hulu cave	6	42	PD	44	H82	10.66	14.91	-6.83	-7.42	0.59
Hulu cave	6	617	MSP	618	MSX	133.19	154.36	-6.86	-6.53	0.33
Lancaster Hole	8	50	LH-70s-1	51	LH-70s-2	6.76	9.72	-4.39	-4.22	0.18
Lancaster Hole	8	50	LH-70s-1	52	LH-70s-3	3.52	8.42	-4.60	-3.76	0.85
Lancaster Hole	8	51	LH-70s-2	52	LH-70s-3	0.97	2.64	-4.00	-3.78	0.23
Lancaster Hole	8	51	LH-70s-2	52	LH-70s-3	2.68	6.73	-4.05	-3.84	0.21
Lancaster Hole	8	51	LH-70s-2	52	LH-70s-3	6.74	8.32	-4.22	-3.70	0.52
Tonnelâ€™naya cave	9	53	TON-1	54	TON-2	8.00	14.43	-7.07	-7.10	0.03
Mawmluh cave	12	61	KM-A	62	MWS-1	5.59	12.35	-6.32	-5.89	0.43
Mawmluh cave	12	61	KM-A	63	MAW-6	6.52	9.68	-6.65	-7.62	0.97
Mawmluh cave	12	61	KM-A	476	ML.1	3.78	4.43	-5.74	-5.82	0.08
Mawmluh cave	12	61	KM-A	477	ML.2	3.67	4.53	-5.89	-5.44	0.45
Mawmluh cave	12	61	KM-A	495	KM-1	6.70	12.31	-6.28	-6.09	0.20
Mawmluh cave	12	62	MWS-1	63	MAW-6	6.53	9.64	-6.63	-7.62	0.99
Mawmluh cave	12	62	MWS-1	63	MAW-6	13.05	15.90	-3.14	-4.82	1.68
Mawmluh cave	12	62	MWS-1	495	KM-1	6.70	22.37	-3.77	-5.33	1.57
Mawmluh cave	12	63	MAW-6	495	KM-1	6.70	9.65	-7.63	-6.48	1.15
Mawmluh cave	12	476	ML.1	477	ML.2	3.78	4.44	-5.82	-5.43	0.39
Ball Gown cave	13	64	BGC-6	635	BGC-11_2017	9.90	11.12	-3.36	-2.69	0.67
Lehman caves	14	641	CDR3	642	WR11	10.22	11.41	-11.52	-11.94	0.42
Huangye cave	17	76	HY1	77	HY2	1.08	1.19	-8.43	-8.66	0.23
Secret cave	20	83	SC02	84	SC03	37.44	54.95	-8.54	-8.51	0.04
Secret cave	20	83	SC02	84	SC03	61.70	77.98	-9.25	-9.21	0.04
Uamh an Tartair	21	85	SU967	86	SU032	-0.04	0.27	-4.36	-4.72	0.36
RukieSSa cave	22	87	Merc-1	88	Asfa-3	-0.05	0.05	-1.27	-1.15	0.12
Lapa sem fim cave	24	92	LSF3_2015	604	LSF3_2018	17.31	19.27	-6.23	-6.25	0.02
Palestina cave	25	93	PAL3	94	PAL4	0.10	0.84	-7.09	-7.21	0.12
Okshola cave	26	95	FM3	96	Oks82	5.10	7.41	-6.57	-6.98	0.42
Mairs cave	29	101	MC-S1	102	MC-S2	15.50	17.16	-6.45	-5.71	0.74
Dongge cave	39	114	D3	115	D4_2004	113.00	148.20	-6.22	-6.90	0.67
Dongge cave	39	115	D4_2004	442	DA_2005	0.14	8.88	-8.31	-8.00	0.31
Dongge cave	39	115	D4_2004	446	D4_2005	0.14	15.78	-7.73	-8.12	0.39
Dongge cave	39	442	DA_2005	446	D4_2005	0.00	8.87	-8.00	-8.37	0.37

Sahiya cave	54	478	SAH-2	480	SAH-6	3.09	3.56	-9.29	-9.28	0.01
Sieben Hengste cave	55	134	7H-2	135	7H-3	17.14	23.52	-12.36	-12.03	0.33
Soylegrotta cave	57	137	SG95	435	SG93	0.48	4.07	-7.30	-7.58	0.29
Whiterock cave	65	685	WR12-01	686	WR12-12	115.81	144.23	-8.27	-8.13	0.13
Abaco Island cave	70	155	AB-DC-01	158	AB-DC-09	23.85	28.80	-2.85	-2.37	0.48
Baradla cave	71	159	BAR-II#L	160	BAR-II#B	109.90	127.96	-6.97	-7.07	0.11
Dim cave	79	169	Dim-E3	170	Dim-E4	12.66	14.39	-4.91	-5.48	0.58
Gueldaman cave	81	173	stm2	174	stm4	4.05	5.77	-5.74	-5.05	0.69
Anjohibe	94	187	AB3	188	AB2	0.29	1.06	-6.15	-5.63	0.52
Anjohibe	94	187	AB3	189	MA3	0.66	1.58	-5.86	-5.59	0.27
Anjohibe	94	187	AB3	190	ANJB-2	1.01	1.57	-5.60	-5.85	0.25
Anjohibe	94	188	AB2	189	MA3	0.65	1.07	-5.79	-6.03	0.24
Anjohibe	94	189	MA3	190	ANJB-2	1.01	1.58	-5.22	-5.85	0.63
Katerloch cave	100	199	K1	200	K3	7.79	10.03	-6.50	-6.26	0.24
Liang Luar cave	104	204	LR06-B1_2009	205	LR06-B3_2009	0.05	2.81	-6.32	-6.17	0.15
Liang Luar cave	104	204	LR06-B1_2009	205	LR06-B3_2009	3.73	6.42	-6.03	-6.23	0.20
Liang Luar cave	104	204	LR06-B1_2009	205	LR06-B3_2009	8.59	10.61	-5.25	-5.25	0.00
Liang Luar cave	104	204	LR06-B1_2009	367	LR06-B3_2013	0.05	2.76	-6.33	-6.17	0.16
Liang Luar cave	104	204	LR06-B1_2009	367	LR06-B3_2013	3.64	6.43	-6.03	-6.22	0.19
Liang Luar cave	104	204	LR06-B1_2009	367	LR06-B3_2013	8.55	10.70	-5.23	-5.26	0.03
Liang Luar cave	104	204	LR06-B1_2009	368	LR06-C2	10.05	12.62	-4.66	-4.54	0.11
Liang Luar cave	104	204	LR06-B1_2009	370	LR06-C5	10.14	12.62	-4.65	-4.71	0.05
Liang Luar cave	104	205	LR06-B3_2009	226	LR06-B1_2016	0.05	1.90	-6.16	-6.19	0.03
Liang Luar cave	104	205	LR06-B3_2009	227	LR06-B3_2016	0.05	1.90	-6.16	-6.23	0.08
Liang Luar cave	104	205	LR06-B3_2009	367	LR06-B3_2013	0.05	10.61	-5.96	-5.97	0.01
Liang Luar cave	104	226	LR06-B1_2016	367	LR06-B3_2013	0.05	1.94	-6.19	-6.16	0.03
Liang Luar cave	104	227	LR06-B3_2016	367	LR06-B3_2013	0.05	1.94	-6.24	-6.16	0.08
Liang Luar cave	104	368	LR06-C2	370	LR06-C5	10.14	13.55	-4.54	-4.69	0.15

Liang Luar cave	104	368	LR06-C2	371	LR06-C6	11.95	13.55	-4.63	-4.79	0.15
Liang Luar cave	104	369	LR06-C3_2013	371	LR06-C6	20.70	23.51	-5.07	-5.25	0.18
Liang Luar cave	104	370	LR06-C5	371	LR06-C6	11.95	13.72	-4.68	-4.76	0.09
Liang Luar cave	104	370	LR06-C5	371	LR06-C6	14.43	17.04	-5.00	-5.07	0.07
Molinos cave	109	216	MO-1	217	MO-7	4.91	6.69	-7.37	-7.44	0.08
Rainha cave	111	219	RN1	220	RN4	4.42	12.32	-5.81	-5.86	0.05
Bukit Assam cave	116	237	BA04	238	BA03_decadal	0.15	4.30	-9.30	-9.46	0.16
Bukit Assam cave	116	237	BA04	238	BA03_decadal	6.17	9.92	-8.68	-8.88	0.20
Bukit Assam cave	116	237	BA04	238	BA03_decadal	10.56	11.83	-7.80	-7.79	0.01
Bukit Assam cave	116	237	BA04	239	BA02	15.25	19.41	-6.83	-8.31	1.49
Bukit Assam cave	116	237	BA04	239	BA02	20.15	26.07	-7.17	-8.65	1.49
Bunker cave	117	240	Bu1	242	Bu4	0.15	6.64	-5.78	-5.69	0.09
Clearwater cave	118	246	FC12-14	247	FC12-15	139.93	155.81	-8.07	-8.56	0.50
Cueva de Asiul	119	248	ASR	249	ASM	0.51	2.10	-5.38	-5.09	0.29
Milchbach cave	123	255	MB-2	256	MB-3	3.25	4.86	-8.00	-7.91	0.09
Milchbach cave	123	255	MB-2	256	MB-3	5.15	6.82	-8.26	-8.33	0.06
Milchbach cave	123	255	MB-2	257	MB-5	5.15	6.82	-8.26	-8.59	0.33
Milchbach cave	123	256	MB-3	257	MB-5	3.97	7.24	-8.28	-8.47	0.19
Xiaobailong cave	127	263	XBL-3	268	XBL-29	30.30	41.32	-11.02	-11.49	0.48
Xiaobailong cave	127	266	XBL-26	269	XBL-48	77.26	106.40	-12.27	-12.20	0.07
Buckeye creek	128	271	BCC-2	272	BCC-4	0.13	1.33	-6.05	-6.15	0.09
Buckeye creek	128	271	BCC-2	272	BCC-4	2.24	6.91	-5.97	-5.84	0.13
Buckeye creek	128	271	BCC-2	273	BCC-6	0.10	6.91	-5.99	-5.97	0.03
Buckeye creek	128	272	BCC-4	273	BCC-6	2.60	7.13	-5.83	-5.92	0.09
Buckeye creek	128	275	BCC-10_2014	682	BCC-10_2019	47.32	123.61	-5.32	-5.32	0.00
Buckeye creek	128	681	BCC-9	683	BCC-30	263.11	328.24	-5.77	-5.62	0.15
Kleegruben cave	132	280	SPA_126	281	SPA_49	47.82	55.97	-12.98	-13.00	0.02
Kinderlinskaya cave	137	290	KC-1	291	KC-3	1.84	4.13	-11.17	-11.17	0.00
Kinderlinskaya cave	137	290	KC-1	291	KC-3	7.21	7.98	-12.46	-12.30	0.15
Kinderlinskaya cave	137	290	KC-1	291	KC-3	8.21	11.66	-13.34	-13.35	0.01
Sanbao cave	140	295	SB-10_2009	296	SB-26_2009	2.13	2.81	-9.20	-9.31	0.11
Sanbao cave	140	295	SB-10_2009	297	SB-27	2.37	8.44	-10.32	-9.92	0.40

Sanbao cave	140	295	SB-10_2009	298	SB-43	2.13	11.51	-10.18	-9.92	0.26
Sanbao cave	140	295	SB-10_2009	299	SB-44	6.96	11.49	-10.23	-9.96	0.27
Sanbao cave	140	295	SB-10_2009	300	SB-49	10.22	11.51	-9.65	-9.80	0.15
Sanbao cave	140	296	SB-26_2009	297	SB-27	2.37	5.19	-9.74	-9.43	0.31
Sanbao cave	140	296	SB-26_2009	298	SB-43	0.46	5.19	-9.46	-9.24	0.22
Sanbao cave	140	297	SB-27	298	SB-43	2.40	8.44	-9.93	-9.80	0.12
Sanbao cave	140	297	SB-27	299	SB-44	6.96	8.44	-10.48	-10.29	0.19
Sanbao cave	140	298	SB-43	299	SB-44	7.66	12.83	-9.81	-9.46	0.35
Sanbao cave	140	298	SB-43	300	SB-49	10.23	12.83	-9.09	-9.32	0.23
Sanbao cave	140	299	SB-44	300	SB-49	10.26	13.15	-9.09	-9.33	0.24
Sanbao cave	140	302	SB-14	303	SB-32	503.80	623.80	-8.69	-8.95	0.26
Sanbao cave	140	484	SB11	487	SB24	155.71	209.02	-9.03	-7.96	1.07
Sanbao cave	140	484	SB11	493	SB42	135.10	187.74	-8.94	-8.59	0.35
Sanbao cave	140	485	SB22	488	SB25-1	78.11	96.09	-8.97	-9.89	0.92
Sanbao cave	140	486	SB23	492	SB41	108.31	129.94	-9.44	-8.89	0.54
Sanbao cave	140	487	SB24	493	SB42	156.88	187.74	-8.32	-8.72	0.40
Sofular cave	141	305	SO-1	456	SO-2	0.05	7.91	-8.26	-8.06	0.20
Sofular cave	141	305	SO-1	456	SO-2	10.04	20.74	-12.08	-11.82	0.26
Sofular cave	141	305	SO-1	456	SO-2	35.13	50.27	-12.42	-12.11	0.32
Sofular cave	141	305	SO-1	687	SO-4	1.75	49.31	-10.53	-11.42	0.89
Sofular cave	141	429	SO-17A	688	SO-6	93.41	109.49	-8.80	-8.98	0.18
Sofular cave	141	456	SO-2	687	SO-4	1.75	7.77	-8.06	-8.09	0.03
Sofular cave	141	456	SO-2	687	SO-4	10.47	20.24	-11.88	-11.63	0.25
Sofular cave	141	456	SO-2	687	SO-4	35.24	59.46	-11.84	-11.63	0.21
BotuverÃ¡ cave	144	311	BTV21a	312	BT-2	0.31	9.16	-3.25	-2.61	0.64
Antro del Corchia	145	313	CC-1_2004	314	CC-5_2005	125.94	139.57	-4.75	-5.00	0.25
Antro del Corchia	145	313	CC-1_2004	317	CC-5_2009	125.94	139.77	-4.75	-5.08	0.33
Antro del Corchia	145	313	CC-1_2004	666	CC-5_2018	126.24	139.79	-4.73	-5.08	0.35
Antro del Corchia	145	314	CC-5_2005	315	CC-28_2007	95.83	117.47	-4.14	-4.33	0.19
Antro del Corchia	145	314	CC-5_2005	316	CC-1_2009	128.01	145.58	-4.82	-4.58	0.24

Antro del Corchia	145	314	CC-5_2005	317	CC-5_2009	125.44	149.54	-4.87	-4.86	0.01
Antro del Corchia	145	314	CC-5_2005	666	CC-5_2018	109.20	124.24	-4.24	-4.28	0.04
Antro del Corchia	145	314	CC-5_2005	666	CC-5_2018	126.17	139.46	-5.02	-5.09	0.07
Antro del Corchia	145	316	CC-1_2009	317	CC-5_2009	128.01	148.26	-4.55	-4.14	0.41
Antro del Corchia	145	317	CC-5_2009	666	CC-5_2018	125.98	139.62	-5.09	-5.06	0.03
Gunung-buda cave (snail shell cave)	146	319	SSC01	320	SCH02	4.00	5.88	-9.92	-9.95	0.04
Gunung-buda cave (snail shell cave)	146	319	SSC01	320	SCH02	13.04	14.76	-7.55	-7.79	0.24
Gunung-buda cave (snail shell cave)	146	319	SSC01	320	SCH02	16.64	21.22	-7.53	-7.55	0.03
Jiuxian cave	154	329	C996-1	330	C996-2	0.04	5.65	-9.01	-9.26	0.26
Munagamanu cave	157	348	Mun-stm2	349	Mun-stm1	0.28	0.68	-6.37	-6.25	0.12
Gardener's Gut	163	357	GG1	358	GG2	1.14	9.55	-3.94	-4.11	0.17
Forestry cave	181	392	10FC-02	393	05FC-04	-0.03	0.07	-7.24	-7.11	0.13
Cold Water cave	190	405	CWC-1s	406	CWC-2ss	1.19	7.41	-5.68	-6.47	0.79
Cold Water cave	190	405	CWC-1s	407	CWC-3l	2.03	7.64	-5.60	-6.12	0.52
Cold Water cave	190	406	CWC-2ss	407	CWC-3l	2.06	7.36	-6.46	-6.12	0.34
Devil's Icebox cave	191	408	DIB-1	409	DIB-2	1.91	3.53	-4.82	-5.02	0.20
Dark cave	216	461	D1	462	D2	1.86	5.75	-8.57	-8.53	0.04
Nuanhe cave	218	465	NH6	466	NH33	7.77	8.65	-9.17	-10.71	1.54
Chiflonkhakha cave	225	497	Boto 1	498	Boto 3	0.23	0.35	-10.22	-10.19	0.03
Chiflonkhakha cave	225	498	Boto 3	499	Boto 7	0.23	0.29	-10.33	-10.84	0.51
Cueva del Tigre Perdido	235	514	NC-A	515	NC-B	3.28	4.27	-7.08	-6.87	0.21
Gempa bumi cave	241	523	GB09-03	524	GB11-09	26.10	39.87	-6.65	-6.37	0.28
Haozhu cave	242	525	HZZ-11	526	HZZ-27	9.44	20.79	-7.83	-8.01	0.18
Lianhua cave, Shanxi	244	528	LH1	532	LH9	1.31	2.77	-9.03	-8.86	0.16
Lianhua cave, Shanxi	244	529	LH4	530	LH5	5.79	6.89	-10.29	-10.18	0.12

Lianhua cave, Shanxi	244	530	LH5	531	LH6	3.27	3.61	-9.11	-9.21	0.09
Lianhua cave, Shanxi	244	530	LH5	532	LH9	3.28	3.77	-9.09	-8.78	0.30
Lianhua cave, Shanxi	244	531	LH6	532	LH9	2.95	3.61	-9.15	-8.90	0.25
Lianhua cave, Shanxi	244	532	LH9	533	LH30	2.45	3.28	-8.94	-9.30	0.37
Shenqi cave	248	538	SQ1	539	SQ7	0.00	1.25	-9.06	-9.02	0.04
Shigao cave	249	540	SG1	541	SG2	4.19	5.78	-8.73	-8.81	0.08
StraÅ¡na peÄ‡ cave	264	567	SPD-1	568	SPD-2	2.57	3.78	-3.73	-4.27	0.55
El Condor cave	192	592	ELC-A	593	ELC-B	4.28	6.23	-6.65	-6.02	0.63
Huagapo cave	277	597	P00-H2	598	P00-H1	1.05	1.38	-12.89	-12.98	0.09
Huagapo cave	277	599	P09-H1b	600	P10-H5	146.56	169.47	-16.04	-15.92	0.12

Supplementary Table 3: Farmed calcite and dripwater $\delta^{18}O$ values collected at each site between 2008-2017. The calculated fractionation factor between calcite and water is shown for each interval and an overall mean value calculated (termed "Empirical bulk fractionation factor").

Date range (MM/YY)	Drip site	Mean calcite $\delta^{18}O$ (‰VPDB)[a,b]	Mean water $\delta^{18}O$ (‰VSMOW)[a,b]	$\alpha_{calcite-water}$[a]	$1000\ln\alpha_{calcite-water}$ (‰)
10/08-04/11	1A	-3.27±0.09 (3)	-4.09±0.26 (21)	1.0318±0.0003	31.27±0.26
	2B	-3.09±0.10 (2)	-4.10±0.31 (20)	1.0320±0.0003	31.46±0.31
	2E	-3.86±0.10 (2)	-4.76±0.59 (22)	1.0318±0.0006	31.35±0.59
05/11-12/11	2B	-2.90±0.10 (2)	-3.86±0.18 (6)	1.0319±0.0002	31.42±0.18
	2E	-3.80±0.19 (2)	-4.89±0.24 (6)	1.0320±0.0002	31.54±0.24
01/12-10/12	2E	-3.82±0.13 (3)	-4.07±0.08 (5)	1.0312±0.0001	30.71±0.08
06/16-10/17	1A	-2.88±0.01 (2)	-3.78±0.18 (14)	1.0319±0.0002	31.36±0.18
	1IV	-3.47±0.02 (2)	-4.13±0.23 (14)	1.0316±0.0002	31.11±0.23
	2E	-3.80±0.30 (2)	-4.41±0.47 (14)	1.0315±0.0005	31.06±0.47
Empirical bulk fractionation factor for Golgotha Cave (n=18)				1.0318±0.0004	31.28±0.40

[a]±1 standard deviation

[b]Value in brackets indicates number of observations

Supplementary Table 4: Description of paired drip sites and stalagmites. Further detail on flow types and drip rate data are given in ref.[2,31].

Drip ID	Flow type	Stalagmite ID	Stalagmite description
Site 1A	Predominately matrix	GL-S1	Near-uniform diameter candle-stick type stalagmite, indicating consistency in drip rate through time, from chamber 1. White, open columnar fabric during last millennium growth section; closed columnar fabric in preceding growth.
Site 1IV	Matrix plus fracture	GL-S4	Uniform diameter candle-stick type stalagmite from chamber 1. White, open columnar fabric.
Site 2B	Matrix plus underflow from secondary store (see also ref[32])	GL-S2	Approximately uniform width boss-type stalagmite from chamber 2. Gour features on sides indicative of faster flow during past. Closed, columnar fabric.
Site 2E	Combination	GL-S3	Irregular width boss-type stalagmite from chamber 2. Gour features on sides indicative of faster flow during past. Closed, columnar fabric.

Supplementary Table 5: Summary of techniques used to construct chronologies for Golgotha Cave speleothems. Data from bomb pulse model previously published in ref.[11]. ADM is age-depth model.

Speleothem	Growth interval (CE)*	Comment
GL-S1	1920-2005: bomb pulse ADM and year of collection (2005). 1000-1920: U/Th age ADM (17th percentile used)	In Figure S5, the 17th percentile ADM is used to align $\delta^{18}O$ maxima with the GL-S4 $\delta^{18}O$ record. This shifts the record 45 years younger at the oldest end of the record shown.
GL-S2	1330-2005: Combined ADM using laminae count scaled to two tie-points (1950 CE in the bomb pulse ADM and the year of collection 2005) and U/Th ages measurements.	Hiatus at 32.6 mm determined from visible feature and bracketing age measurements. Laminae count based on a Sr line scan extracted from synchrotron XFM created for 0-13.6 mm. The Sr laminae were visible in the XFM image for GL-S2 but of insufficient clarity to confidently visualise growth laminae across the width of the map owing to the 'fuzzy' appearance of the bands. Thus the laminae count was based on three 'line scans' extracted from the map using ImageJ and counting the common peaks in Sr across the three lines rather than the preferred method of counting the Sr laminae by detection of continuous laminae features across the map. As a chross-check the laminae count was compared to the bomb pulse ADM and as a result scaled to 88(±12)%. This is consistent with the tendency for more 'false' Sr peaks to be encountered in line scans versus the 2D map.
GL-S3	1950-2008: mean laminae growth rate (69±11 μm/a; laminae were present for 27% of growth) and year of collection (2008). 1200-1360: Combined U/Th ADM and laminae counting. Mean laminae growth rate (96±27 μm/a) determined from laminae over 1270-1360 interval.	Hiatus at 4.2 mm depth determined from visible feature. Lack of deposition below 1200 CE determined from bracketing radiometric ages and visible hiatus at 21.5 mm depth.
GL-S4	1200-2012: Sr laminae counting and year of collection. Laminae ADM published in ref[33].	Laminae chronology is supported by both bomb pulse ADM and U/Th ages. Hiatus at 46.4 mm indicated by detrital layer and supported by bracketing ages.

*Median ages: see Supplementary Figure 4 for ADM uncertainties.

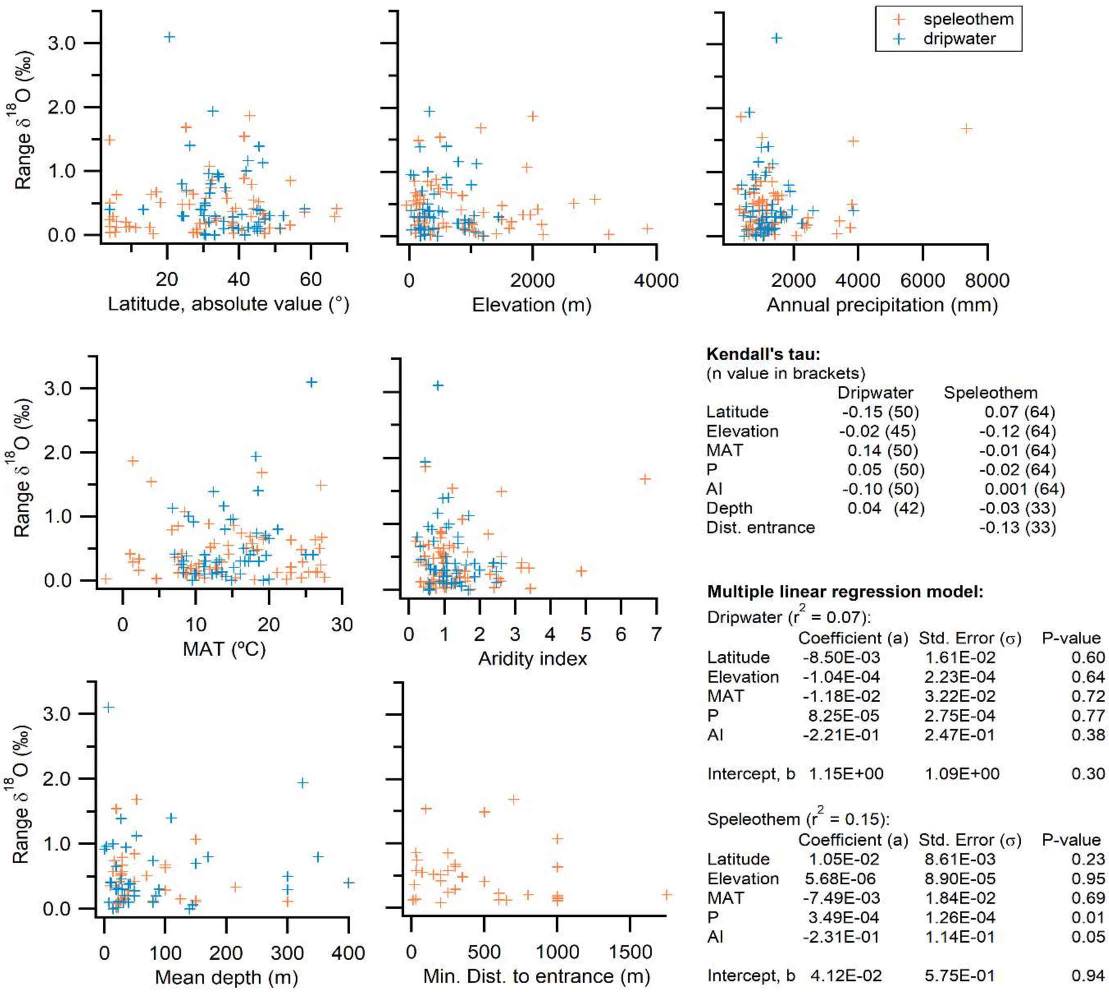

Kendall's tau:
(n value in brackets)

	Dripwater	Speleothem
Latitude	-0.15 (50)	0.07 (64)
Elevation	-0.02 (45)	-0.12 (64)
MAT	0.14 (50)	-0.01 (64)
P	0.05 (50)	-0.02 (64)
AI	-0.10 (50)	0.001 (64)
Depth	0.04 (42)	-0.03 (33)
Dist. entrance		-0.13 (33)

Multiple linear regression model:

Dripwater (r^2 = 0.07):

	Coefficient (a)	Std. Error (σ)	P-value
Latitude	-8.50E-03	1.61E-02	0.60
Elevation	-1.04E-04	2.23E-04	0.64
MAT	-1.18E-02	3.22E-02	0.72
P	8.25E-05	2.75E-04	0.77
AI	-2.21E-01	2.47E-01	0.38
Intercept, b	1.15E+00	1.09E+00	0.30

Speleothem (r^2 = 0.15):

	Coefficient (a)	Std. Error (σ)	P-value
Latitude	1.05E-02	8.61E-03	0.23
Elevation	5.68E-06	8.90E-05	0.95
MAT	-7.49E-03	1.84E-02	0.69
P	3.49E-04	1.26E-04	0.01
AI	-2.31E-01	1.14E-01	0.05
Intercept, b	4.12E-02	5.75E-01	0.94

Supplementary Figure 1: Cross-plots of within cave range in mean dripwater or coeval speleothem $\delta^{18}O$ data with latitude, elevation, annual precipitation, mean annual temperature, aridity index (AI; precipitation divided by actual evapotranspiration) mean depth, and minimum distance from cave entrance. Also shown are Kendall's tau values for each variable ranked against within cave range $\delta^{18}O$; and output from multiple linear regression models (MLR) for dripwater and speleothem datasets for climate variables or variables sensitive to climate (latitude and elevation). The MLR is represented as $y=(a_1\pm\sigma_1)x_1 + (a_2\pm\sigma_2)x_2 + \ldots + (a_n\pm\sigma_n)x_n + (b\pm\sigma)$ for variables 1 to n. The engineering notation used in the MLR output is base 10 e.g. -8.50E-03 is equivalent to -8.5×10^{-3}. Overall, the models explain 7% and 15% of the variation in the within cave range $\delta^{18}O$, for dripwater and speleothem datasets. There are weak to no relationships between the within cave range of mean dripwater and coeval speleothem $\delta^{18}O$ values and these variables (Kendall's tau; 0.05) and the P-values indicate that none of the relationships in the multiple linear regression model are significant. There is also no relationship between the intra-cave range $\delta^{18}O$ and the minimum distance from the cave entrance to either coeval stalagmite pair in the SISAL data suggesting that the discrepancy between coeval speleothem mean values is not related to the stability of the climate inside the cave. This analysis suggests that karst hydrological heterogeneity is important over all climate types, cave depths and host rock types. Mean depth is the estimated mean thickness of host rock above site of dripwater monitoring or collected speleothem. Cave meta-data were extracted from SISAL V2[34] and climate variables from

WorldClim V1[35]. Cave depth and distance to entrance data were not available for all sites. In cases where elevation data were not provided, these were taken from ref[36].

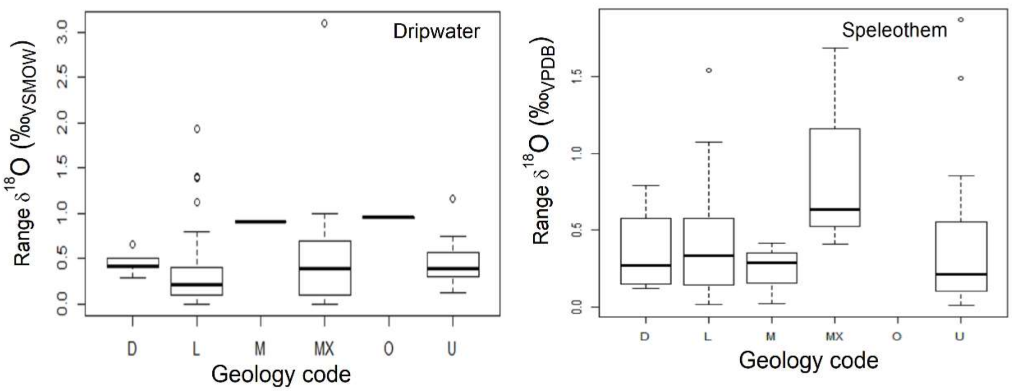

Supplementary Figure 2: Mann-Whitney U test for within-cave range in mean $\delta^{18}O$ and geology type. Geology codes: D is dolomite, L is limestone, M is marble, MX is mixed, O is 'other' and U is unknown. There were no significant differences in median values for different host rock types using a p-value = 0.05 for either the dripwater or speleothem datasets. For dripwaters, the differences significant at p-value = 0.1 between dolomite and 'other' although 'other' had a small number of values; and between limestone and 'unknown' although there is an overlap of the distributions.

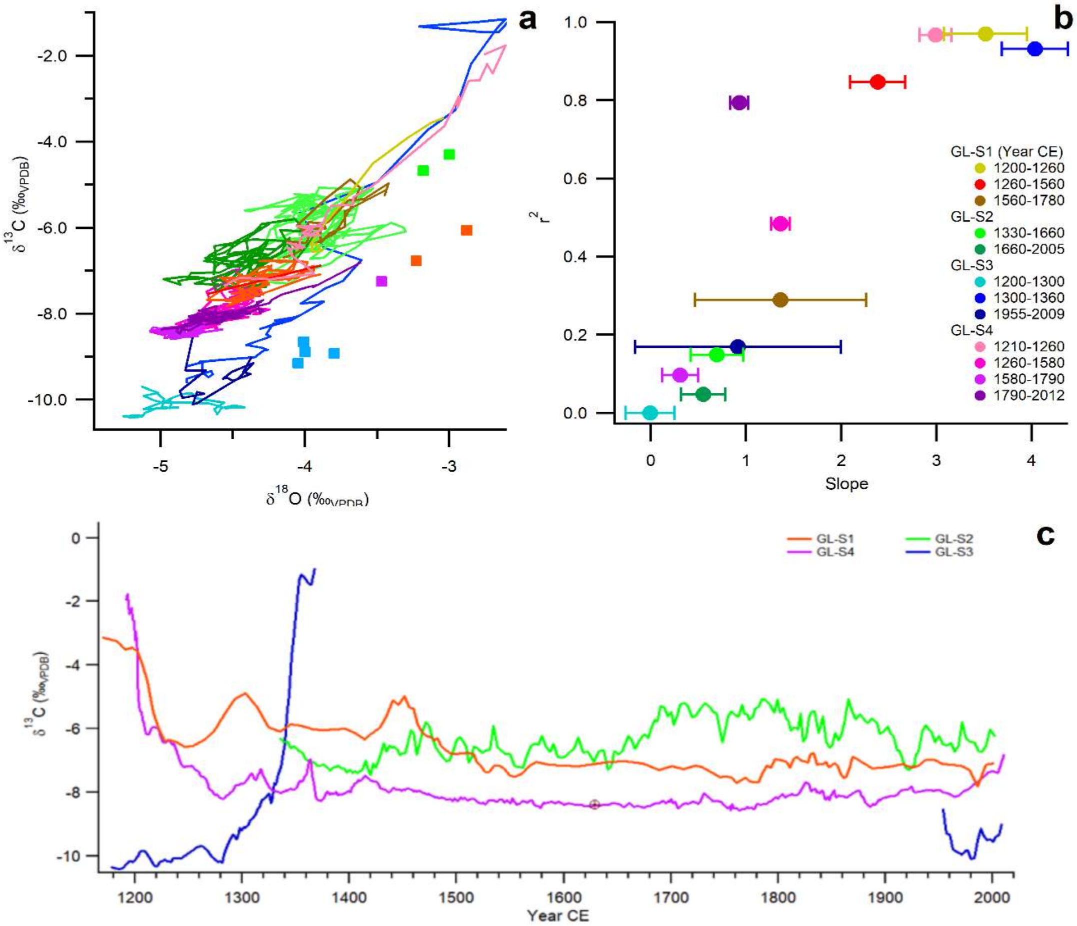

Supplementary Figure 3a-c. Scatterplots of speleothem δ^{13}C versus δ^{18}O for Golgotha speleothems (a); Pearson's r^2 value versus slope for intervals chosen from panel a with different slope and r^2 values (b); and δ^{13}C time series (c). Farmed calcites (square symbols) also appear on (a) for comparison. Colour-coding on legend on (b) applies to both plots. Intervals with lowest δ^{18}O values (highest fracture flow influence) have weakest relationships between speleothem δ^{13}C and δ^{18}O values.

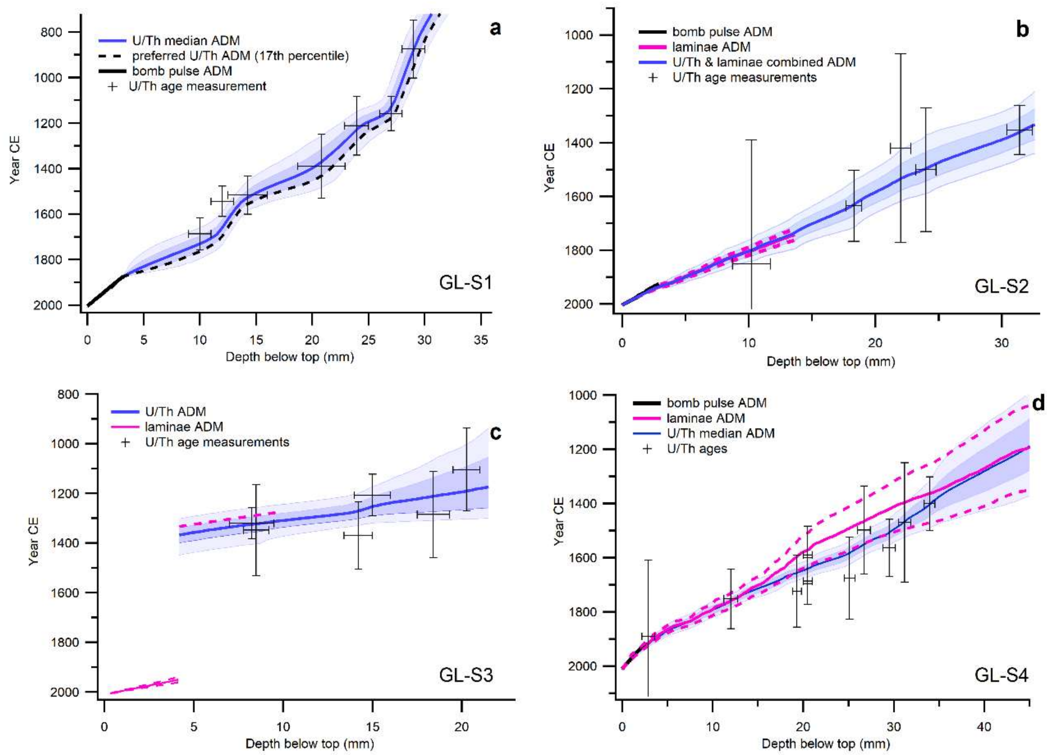

Supplementary Figure 4a-d. Age-depth models for each stalagmite based on U/Th age measurements and bomb pulse models for stalagmites GL-S1 (a), GL-S2 (b), GL-S3 (c) and GL-S4 (d). Also shown are age-depth models derived from Sr concentration laminae and bomb pulse ADM. Uncertainty on bomb pulse ADM is +/-0.05 mm and +/-0.004 ka.

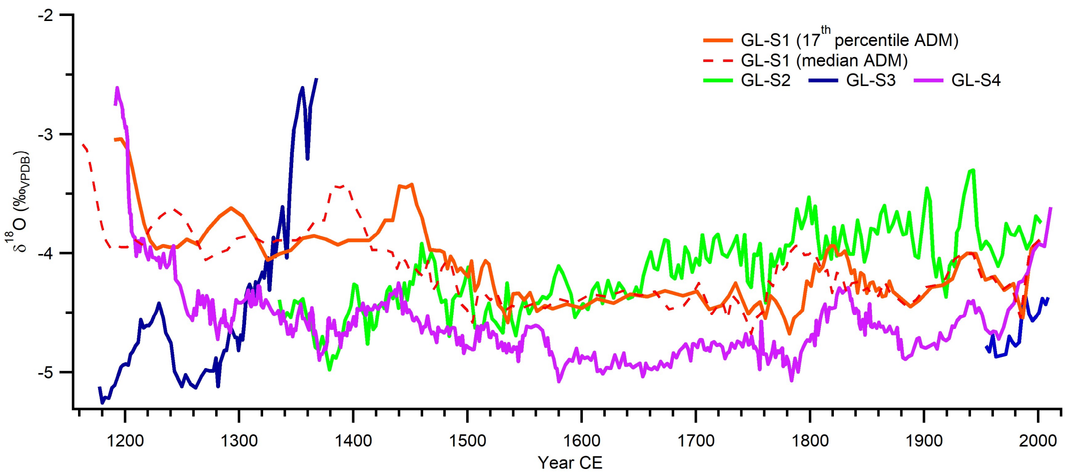

Supplementary Figure 5: Stalagmite $\delta^{18}O$ data shown with GL-S1 plotted using the 17^{th} and 50^{th} percentile U/Th age-depth models. GL-S1 $\delta^{18}O$ plotted on the 17^{th} percentile ADM closely follows GL-S4 $\delta^{18}O$. GL-S4 chronology is based on laminae counting. A summary of the construction of each chronology is in Table S5.

Supplementary References

1. Markowska, M. *et al.* Modern speleothem oxygen isotope hydroclimate records in water-limited SE Australia. *Geochim Cosmochim Ac* **270**, 431-448, doi:https://doi.org/10.1016/j.gca.2019.12.007 (2020).
2. Mahmud, K., Mariethoz, G., Treble, P. C. & Baker, A. Terrestrial LiDAR survey and morphological analysis to identify infiltration properties in the Tamala Limestone, Western Australia. *IEEE Journal of Selected Topics in Applied Earth Observations and Remote Sensing* **8**, 4871-4881, doi:10.1109/JSTARS.2015.2451088 (2015).
3. Gat, J. R. Oxygen and Hydrogen Isotopes in the Hydrologic Cycle. *Annual Review of Earth and Planetary Sciences* **24**, 225-262, doi:10.1146/annurev.earth.24.1.225 (1996).
4. Horita, J. & Wesolowski, D. J. Liquid-vapor fractionation of oxygen and hydrogen isotopes of water from the freezing to the critical temperature. *Geochim Cosmochim Ac* **58**, 3425-3437 (1994).
5. Frisia, S. & Borsato, A. in *Developments in Sedimentology* Vol. 61 (eds A. M. Alonso-Zarza & L. H. Tanner) 269-318 (Elsevier, 2010).
6. Mickler, P. J., Stern, L. A. & Banner, J. L. Large kinetic isotope effects in modern speleothems. *Geological Society Of America Bulletin* **118**, 65-81 (2006).
7. Paterson, D. *et al.* in *The 10th International Conference On X-Ray Microscopy* 219-222 (AIP Publishing, 2011).
8. Wang, J. K. *et al.* Hydroclimatic variability in Southeast Asia over the past two millennia. *Earth and Planetary Science Letters* **525**, 115737, doi:https://doi.org/10.1016/j.epsl.2019.115737 (2019).
9. Faraji, M. *et al.* Accurate dating of stalagmites from low seasonal contrast tropical Pacific climate using Sr 2D maps, fabrics and annual hydrological cycles. *Sci Rep-Uk* **11**, 2178, doi:10.1038/s41598-021-81941-x (2021).
10. Hellstrom, J. Rapid and accurate U/Th dating using parallel ion-counting multi-collector ICP-MS. *Journal of Analytical Atomic Spectrometry* **18**, 1346-1351, doi:10.1039/b308781f (2003).
11. Markowska, M. *et al.* Modelling the 14C bomb-pulse in young speleothems using a soil carbon continuum model. *Geochim Cosmochim Ac* **261**, 342-367, doi:https://doi.org/10.1016/j.gca.2019.04.029 (2019).
12. Baker, A. *et al.* Global analysis reveals climatic controls on the oxygen isotope composition of cave drip water. *Nat Commun* **10**, 2984, doi:10.1038/s41467-019-11027-w (2019).
13. Yin, J.-J. *et al.* Individual event, seasonal and interannual variations in δ18O values of drip water in Maomaotou Big Cave, Guilin, South China, and their implications for palaeoclimatic reconstructions. **n/a**, doi:10.1111/bor.12454 (2020).
14. Czuppon, G., Bočić, N., Buzjak, N., Óvári, M. & Molnár, M. Monitoring in the Barać and Lower Cerovačka caves (Croatia) as a basis for the characterization of the climatological and hydrological processes that control speleothem formation. *Quaternary International* **494**, 52-65, doi:https://doi.org/10.1016/j.quaint.2018.02.003 (2018).
15. Drăguşin, V. *et al.* Transfer of environmental signals from the surface to the underground at Ascunsă Cave, Romania. *Hydrol. Earth Syst. Sci.* **21**, 5357-5373, doi:10.5194/hess-21-5357-2017 (2017).
16. Boch, R. *Stalagmites from Katerloch Cave, Austria: Growth dynamics and high-resolution records of climate change* PhD thesis, Leopold-Franzens-Universitat Innsbruck, (2008).

17 Mattey, D. *et al.* A 53 year seasonally resolved oxygen and carbon isotope record from a modem Gibraltar speleothem: Reconstructed drip water and relationship to local precipitation. *Earth And Planetary Science Letters* **269**, 80-95 (2008).

18 Burstyn, Y. Multi-decadal to seasonal climate change recorded by stable isotope and trace element variability in modern cave-waters and calcite of Soreq Cave, Israel. 107 (The Hebrew University of Jerusalem, Jerusalem, 2013).

19 Ayalon, A., Bar-Mathews, M. & Sass, E. Rainfall-recharge relationships within a karstic terrain within the Eastern Mediterranean semi-arid region, Israel: d18O and dD charateristics. *Journal of Hydrology* **207**, 18-30 (1998).

20 Lambert, W. J. & Aharon, P. Oxygen and hydrogen isotopes of rainfall and dripwater at DeSoto Caverns (Alabama, USA): Key to understanding past variability of moisture transport from the Gulf of Mexico. *Geochimica et Cosmochimica Acta* **74**, doi:10.1016/j.gca.2009.10.043 (2010).

21 van Beynen, P. & Febbroriello, P. Seasonal isotopic variability of precipitation and cave drip water at Indian Oven Cave, New York. *Hydrological Processes* **20**, 1793-1803 (2006).

22 Chapman, J. B., Ingraham, N. L. & Hess, J. W. Isotopic investigation of infiltration and unsaturated zone flow processes at Carlsbad Cavern, New Mexico. *Journal of Hydrology* **133**, 343-363, doi:https://doi.org/10.1016/0022-1694(92)90262-T (1992).

23 Cruz, F. W. *et al.* Stable isotope study of cave percolation waters in subtropical Brazil: Implications for paleoclimate inferences from speleothems. *Chemical Geology* **220**, 245-262 (2005).

24 Bian, F. *et al.* Hydrological and geochemical responses of fire in a shallow cave system. *Science of The Total Environment* **662**, 180-191, doi:https://doi.org/10.1016/j.scitotenv.2019.01.102 (2019).

25 Coleborn, K. *et al.* The impact of fire on the geochemistry of speleothem-forming drip water in a sub-alpine cave. *Science of The Total Environment* **642**, 408-420, doi:https://doi.org/10.1016/j.scitotenv.2018.05.310 (2018).

26 Coleborn, K. *et al.* Corrigendum to "The impact of fire on the geochemistry of speleothem-forming drip water in a sub-alpine cave" [Sci. Total Environ. (2018) 408–420]. *Science of The Total Environment* **668**, 1339-1340, doi:https://doi.org/10.1016/j.scitotenv.2019.02.350 (2019).

27 Nagra, G. *et al.* A post-wildfire response in cave dripwater chemistry. *Hydrol Earth Syst Sc* **20**, 2745-2758, doi:10.5194/hess-20-2745-2016 (2016).

28 Williams, P. W. & Fowler, A. Relationship between oxygen isotopes in rainfall, cave percolation waters and speleothem calcite at Waitomo, New Zealand. *Journal of Hydrology (New Zealand)* **41**, 53-70 (2002).

29 Nava-Fernandez, C. *et al.* Pacific climate reflected in Waipuna Cave drip water hydrochemistry. *Hydrol. Earth Syst. Sci.* **24**, 3361-3380, doi:10.5194/hess-24-3361-2020 (2020).

30 Comas-Bru, L. *et al.* SISALv2: a comprehensive speleothem isotope database with multiple age–depth models. *Earth Syst. Sci. Data* **12**, 2579-2606, doi:10.5194/essd-12-2579-2020 (2020).

31 Mahmud, K. *et al.* Estimation of deep infiltration in unsaturated limestone environments using cave LiDAR and drip count data. *Hydrological and Earth System Sciences* **20**, 359-373, doi:doi:10.5194/hess-20-359-2016 (2016).

32 Treble, P. C. *et al.* An isotopic and modelling study of flow paths and storage in Quaternary calcarenite, SW Australia: implications for speleothem paleoclimate records. *Quaternary Science Reviews* **64**, 90-103, doi:http://dx.doi.org/10.1016/j.quascirev.2012.12.015 (2013).

33 Baker, A. *et al.* The properties of annually laminated stalagmites - a global synthesis. **n/a**, e2020RG000722, doi:https://doi.org/10.1029/2020RG000722.

34 Comas-Bru, L. *et al.* SISALv2: A comprehensive speleothem isotope database with multiple age-depth models. *Earth Syst. Sci. Data* **12**, 2579-2606, doi:10.5194/essd-12-2579-2020 (2020).

35 Hijmans, R. J., Cameron, S. E., Parra, J. L., Jones, P. G. & Jarvis, A. (2004).

36 Spotl, C., Moseley, G., Johnson, K., Mattey, D. & P., T. *Cave monitoring database*, <www.cave-monitoring.org> (2020).